

Suzaku observations of the Hydra A cluster out to the virial radius

Takuya SATO¹, Toru SASAKI¹, Kyoko MATSUSHITA¹, Eri SAKUMA¹, Kosuke SATO¹,
Yutaka FUJITA², Nobuhiro OKABE³, Yasushi FUKAZAWA⁴, Kazuya ICHIKAWA¹,
Madoka KAWAHARADA⁵, Kazuhiro NAKAZAWA⁶, Takaya OHASHI⁷, Naomi OTA⁸,
Motokazu TAKIZAWA⁹, and Takayuki TAMURA⁵

¹*Department of physics, Tokyo University of Science, 1-3 Kagurazaka, Shinjuku-ku, Tokyo 162-8601, Japan*
j1209703@ed.kagu.tus.ac.jp; matusita@rs.kagu.tus.ac.jp

²*Department of Earth and Space Science, Graduate School of Science, Osaka University, Toyonaka, Osaka 560-0043, Japan*

³*Institute of Astronomy and Astrophysics, Academia Sinica, P.O. Box 23-141, Taipei 106, Taiwan; Astronomical Institute, Tohoku University, Aramaki, Aoba-ku, Sendai, 980-8578, Japan*

⁴*Department of Physical Science, Hiroshima University, 1-3-1 Kagamiyama, Higashi-Hiroshima, Hiroshima 739-8526, Japan*

⁵*Institute of Space and Astronautical Science, Japan Aerospace Exploration Agency, 3-1-1 Yoshinodai, Chuo-ku, Sagami-hara, Kanagawa 252-5210, Japan*

⁶*Department of Physics, The University of Tokyo, 7-3-1 Hongo, Bunkyo-ku, Tokyo 113-0033, Japan*

⁷*Department of Physics, Tokyo Metropolitan University, 1-1 Minami-Osawa, Hachioji, Tokyo 192-0397, Japan*

⁸*Department of Physics, Nara Women's University, Kitauoyanishi-machi, Nara, Nara 630-8506, Japan*

⁹*Department of Physics, Yamagata University, Yamagata, Yamagata 990-8560, Japan*

(Received December 15, 2011; accepted March 12, 2012)

Abstract

We report Suzaku observations of the northern half of the Hydra A cluster out to ~ 1.4 Mpc, reaching the virial radius. This is the first Suzaku observations of a medium-size ($kT \sim 3$ keV) cluster out to the virial radius. Two observations were conducted, north-west and north-east offsets, which continue in a filament direction and a void direction of the large-scale structure of the Universe, respectively. The X-ray emission and distribution of galaxies elongate in the filament direction. The temperature profiles in the two directions are mostly consistent with each other within the error bars and drop to 1.5 keV at $1.5 r_{500}$. As observed by Suzaku in hot clusters, the entropy profile becomes flatter beyond r_{500} , in disagreement with the $r^{1.1}$ relationship that is expected from accretion shock heating models. When scaled with the average intracluster medium (ICM) temperature, the entropy profiles of clusters observed with Suzaku are universal and do not depend on system mass. The hydrostatic mass values in the void and filament directions are in good agreement, and the Navarro, Frenk, and White universal mass profile represents the hydrostatic mass distribution up to $\sim 2 r_{500}$. Beyond r_{500} , the ratio of gas mass to hydrostatic mass exceeds the result of the Wilkinson microwave anisotropy probe, and at r_{100} , these ratios in the filament and void directions reach 0.4 and 0.3, respectively. We discuss possible deviations from hydrostatic equilibrium at cluster outskirts. We derived radial profiles of the gas-mass-to-light ratio and iron-mass-to-light ratio out to the virial radius. Within r_{500} , the iron-mass-to-light ratio of the Hydra A cluster was compared with those in other clusters observed with Suzaku.

Key words: galaxies: clusters: individual (Hydra A cluster) — X-rays: galaxies: clusters — intergalactic medium

1. Introduction

Clusters of galaxies are the largest self-gravitating systems in the Universe, and offer unique information on the process of structure formation governed by cold dark matter (CDM). In addition, these clusters are considered as a laboratory for studying thermal and chemical evolutions of the Universe in which baryons play the most important role. X-ray observations provide valuable information about the structure formation, gas heating and cooling, and metal enrichment of galaxy clusters. Because the dynamical time-scale of clusters is comparable to the Hubble time, cluster outskirts should maintain original records of cluster evolution via accretion of gas and substructures from filaments of the surrounding large-scale structure of the Universe.

Thanks to the low and stable background of the X-ray

Imaging Spectrometer (XIS; Koyama et al. 2007), Suzaku (Mitsuda et al. 2007) was able to unveil for the first time the intracluster medium (ICM) beyond r_{500} , a radius within which the mean cluster-mass density is 500 times the cosmic critical density. The accurate calibration of the XIS also allows precise measurements of the ICM temperature (Sato et al. 2011). Suzaku derived the temperature and entropy profiles of the ICM of several massive clusters up to the virial radius (George et al. 2009; Reiprich et al. 2009; Bautz et al. 2009; Kawaharada et al. 2010; Hoshino et al. 2010; Simionescu et al. 2011; Akamatsu et al. 2011). From the center to r_{200} , a systematic drop in temperature was found by a factor of ~ 3 , and the observed entropy profiles become flatter beyond r_{500} . These profiles are lower than the entropy profile predicted by the numerical simulations of gravitational collapse (Tozzi & Norman 2001; Voit, Kay, Bryan 2005), which is pro-

portional to $r^{1.1}$. Kawaharada et al. (2010) discovered that beyond r_{500} of the Abell 1689 cluster, the total mass obtained from weak-lensing observations with Subaru is larger than that calculated assuming hydrostatic equilibrium. Therefore, one explanation for the low entropy profiles at cluster outskirts is that infalling matter retained some of its kinetic energy in bulk motion (Bautz et al. 2009; George et al. 2009; Kawaharada et al. 2010). Based on Suzaku observations of the Perseus cluster, Simionescu et al. (2011) proposed a gas-clumping effect as an additional interpretation. Hoshino et al. (2010) and Akamatsu et al. (2011) discussed possible deviations of electron temperature from ion temperature to explain the observed lower temperature and entropy profiles. To clarify these effects in the outskirts, dependence on the system mass or on the ICM temperature should be examined. With XMM-Newton observations, Urban et al. (2011) found a similar flattening of the entropy profile in one direction in the Virgo cluster ($kT = 2.3$ keV). However, Humphrey et al. (2011) detected no evidence of flat profiles at large scales ($> r_{500}$) in the relaxed fossil group or in the poor cluster, RXJ 1159+5531. Therefore, more samples of medium-sized clusters are required.

In addition to measuring the temperature and entropy profiles, Suzaku measured the abundance of Fe in the ICM beyond $0.5r_{180}$ (Fujita et al. 2008; Tawa et al. 2008; Simionescu et al. 2011). Metal abundances in the ICM also provide important information on the chemical history and evolution of clusters. The ASCA satellite first measured the distribution of Fe in the ICM (Fukazawa et al. 2000; Finoguenov et al. 2001). Recently, spatial distributions of Fe from 0.3 to 0.4 r_{180} have been studied with the XMM-Newton and Chandra satellites (Vikhlinin et al. 2005; Maughan et al. 2008; Leccardi & Molendi 2008; Matsushita 2011). Since metals are synthesized by supernovae (SNe) in galaxies, the ratios of metal mass in the ICM to the total light from galaxies in clusters or groups, (i.e., metal-mass-to-light ratios) are key parameters in investigating the chemical evolution of the ICM. Suzaku measured the iron-mass-to-light ratios (IMLR) of several clusters and galaxy groups out to 0.2 \sim 0.5 r_{180} (Matsushita 2007; Komiyama et al. 2009; Sato et al. 2007; Sato et al. 2008; Sato et al. 2009a; Sato et al. 2009b; Sato et al. 2010; Sakuma et al. 2011), and with XMM-Newton, the IMLR of the Coma cluster out to $0.5r_{180}$ was derived (Matsushita et al. 2011). The IMLR profiles increase with radius, indicating that Fe in the ICM extends farther than stars.

The Hydra A cluster ($z = 0.0539$) with an ICM temperature of ~ 3 keV is one of the prototype cool-core clusters in which McNamara et al (2000) discovered a displacement of X-ray gas in the central region through the radio lobes from the central active galactic nucleus (AGN). This cluster is also known as Abell 780 and remains a major examples of AGN interaction that is studied through radio and X-rays (Taylor et al. 1990; David et al. 2001; Nulsen et al. 2002; Nulsen et al. 2005; Lane et al. 2004; Wise et al. 2007; Simionescu et al. 2009a; Simionescu et al. 2009b; Kirkpatrick et al. 2009). Through Chandra and XMM-Newton observations, a sharp X-ray surface-brightness edge was detected at radii between $4.3'$ and $6'$ (200–300 kpc) and was interpreted as a shock wave caused by an AGN outburst. The abundances of the Hydra A cluster was measured within $\sim 0.3 r_{180}$ with XMM (Simionescu et al. 2009b; Matsushita 2011).

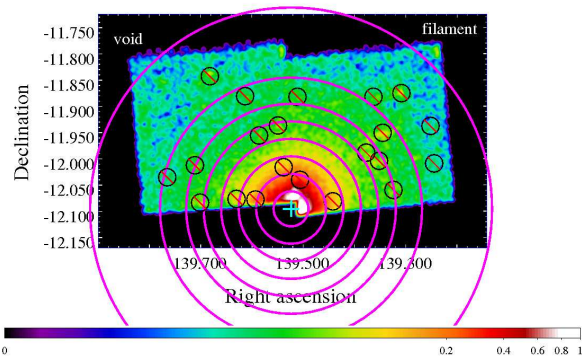


Fig. 1. XIS0 image of the Hydra A cluster within 0.5–4.0 keV energy range. The light blue cross indicates the X-ray peak of the cluster. Differences in the vignetting effect are uncorrected. Regions of spectral accumulation are shown as magenta rings. The ring radii are $2'$, $4'$, $6'$, $8'$, $10'$, $12'$, $15'$ and $23'$. Black circles represent excluded regions around point sources.

This paper reports the results of two Suzaku observations in the northern half of the Hydra A cluster out to $25'$ (≈ 1.5 Mpc), which corresponds to the virial radius. The observations were conducted using the XIS. This study reports the first Suzaku observations of a medium-sized cluster with an average temperature of ~ 3 keV up to the virial radius. The two observed fields continue in a filament direction that continues to the Abell 754 cluster and a void direction of the large-scale structure of the Universe (see Figure 9).

In this study, we use the Hubble constant, $H_0 = 70 \text{ km s}^{-1} \text{ Mpc}^{-1}$, $\Omega_m = 0.27$ and $\Omega_\Lambda = 0.73$. The luminosity distance D_L and angular size distance D_A to the Hydra A cluster are $D_L = 240$ Mpc and $D_A = 217$ Mpc, respectively, and $1'$ corresponds to 66.6 kpc. We use the epoch J2000.0 for the right ascension and declination of the equatorial coordinate system. In addition, we use the solar abundance table by Lodders (2003), in which the solar Fe abundance relative to H is 2.95×10^{-5} . Considering a difference in solar He abundance, the Fe abundance yielded by Lodders (2003) is 1.5 times higher than that using the photo-spheric value by Anders & Grevesse (1989). Errors were quoted at a 90% confidence level for a single parameter.

2. Observation and Data Reduction

2.1. Suzaku observations

Suzaku conducted two observations of the Hydra A cluster in November 2010, which was during the Suzaku Phase-V period. The details of the observations are summarized in Table 1. The first observation, HYDRA A-1, was $12'$ north-west offset from the X-ray peak of the Hydra A cluster with coordinates (RA, Dec) = (139.5236, -12.0955) in degrees. The second observation, HYDRA A-2, was $12'$ north-east offset from the X-ray peak of the Hydra A cluster. The north-west and north-east fields continue into the filament and void structures, respectively (See figure 9). Hereafter, we refer to the north-west and north-east offsets as filament and void, respectively.

Table 1. Observation log of the Hydra A cluster

Field name	Target name	Sequence number	Observation date	RA* (deg)	Dec* (deg)	Exposure (ks)
North-west (filament)	HYDRA A-1	805007010	2010-11-08	139.3723	-11.9472	35.6
North-east (void)	HYDRA A-2	805008010	2010-11-09	139.6749	-11.9472	34.9

* Coordinates are referred to J2000.0.

The XIS, which was operated in its normal mode during the observations, consists of three sets of X-ray CCD (XIS0, XIS1, and XIS3). XIS1 is a back-illuminated (BI) sensor, while both XIS0 and XIS3 are front-illuminated (FI) sensors. Data reduction was done with HEASoft version 6.11. The XIS event lists created by rev 2.5 pipeline processing were filtered using the following additional criteria: a geomagnetic cutoff rigidity (COR2) > 6 GV, and an elevation angle $> 10^\circ$ from the earth limb. The 5×5 and 3×3 editing modes data formats were added. The exposure times after data selection are shown in Table 1.

To obtain the temperature and electron density profiles, we accumulated spectra within annular regions centered on the X-ray peak as shown in Figure 1. Regions around calibration sources and the innermost region within $2'$ were excluded from the spectral analysis. The reason for this exclusion is that we could not obtain sufficient photon statistics to analyze the spectra (which have multiphase features at the cluster center) because the given area was detected on the edge of a CCD chip in our observation. In addition, Suzaku's PSF is also insufficient to resolve such a complex structure. However, with their powerful imaging capability, Chandra and XMM observations have unveiled such complex features in the central region. Using the ewavelet tool in SAS¹, we searched for point-like sources in the Suzaku images in the energy range of 2.0–10.0 keV. In this energy range, the flux levels were approximately $> 2 \times 10^{-14}$ erg cm⁻² s⁻¹. These point sources were excluded as circular regions with radii of $1'$ (figure 1). The non X-ray background (NXB) was subtracted from each spectrum using a database of night Earth observations with the same detector area and COR distribution (Tawa et al. 2008).

We included the degradation of energy resolution due to radiation damage in the redistribution matrix file (RMF) generated by the `xisrmfgen` Ftools task. In addition, we created an ancillary response file (ARF) using the `xissimarfgen` Ftools task (Ishisaki et al. 2007). A decrease in the low-energy transmission of the XIS optical blocking filter (OBF) was also included in the ARF. For filament and void fields, we generated ARF files assuming uniformly extended emission from an enriched region with a $20'$ radius. We used the XSPEC_v12.7.0 package and ATOMDB_v2.0.1 for spectral analysis. Each spectrum was binned and each spectral bin contained a minimum of 50 counts. To avoid systematic uncertainties in the background, we ignored energy ranges above 7 keV and below 0.7 keV. In addition, we excluded the narrow energy band between 1.82 and 1.84 keV in the fits because of the incomplete response around the Si edge.

¹ <http://xmm.esa.int/sas/>

2.2. XMM observations

We used the same data and analysis as that reported by Matsushita (2011). The XMM-Newton archival data of Hydra A (observation identifier 0109980301) had exposure times of 14.0 ks, 19.1 ks and 22.2 ks for MOS1, MOS2 and PN, respectively, after background flares were screened out. We selected events with patterns smaller than 5 and 13 for the PN and MOS, respectively. Spectra were accumulated in concentric annular regions of $0'-0.5'$, $0.5'-1'$, $1'-1.5'$, $1.5'-2'$, $2'-3'$, $3'-4'$, $4'-5'$, $5'-6'$, $6'-7'$, $7'-8'$, and $8'-9'$, centered on the X-ray peak of the Hydra A cluster. Here, the X-ray peaks were derived using the ewavelet tool of SAS-v8.0.0, and luminous point sources were excluded. The spectra from MOS1 and MOS2 were added. The background spectrum for each annular region was calculated by integrating blank-sky data in the same detector region. From deep-sky observations with XMM-Newton, we selected the data having background most similar to that of the Hydra A cluster and the faintest Galactic emission, after screening out background flare events from the data and the background, following Katayama et al. (2004). Next, we scaled the background using a count rate between 10 and 12 keV.

The response matrix file and the ARF corresponding to each spectrum were calculated using SAS-v8.0.0. Further details appear in sections 2 and 3 of Matsushita (2011).

3. Data Analysis

3.1. Estimation of background spectra

To derive the radial profiles of the temperature, electron density, and Fe abundance of the ICM, we fitted the NXB-subtracted spectra with a thermal plasma model (APEC; Smith et al. 2001).

We first fitted the spectra in the outermost ring ($15'-23'$ region) to determine the local X-ray background. As reported by Yoshino et al. (2009), the background emission of Suzaku XIS can be fitted with a three-component model: two thermal plasma models (APEC; Smith et al. 2001) for the local hot bubble (LHB) and the solar wind charge exchange (SWCX), the Milky Way Halo (MWH), and a power-law model for the extragalactic cosmic X-ray background (CXB). MWH and CXB components were convolved with an photoelectric absorption in the Galaxy, N_H . Therefore, we adopted the model formula, $apec_{LHB} + wabs \times (apec_{MWH} + power-law_{CXB})$ as background. We assumed a zero redshift and a solar abundance for LHB and MWH components. The temperature of the LHB and MWH was fixed at 0.1 keV and 0.3 keV, respectively. The column density of the Galactic neutral hydrogen was fixed at 4.7×10^{20} cm⁻² (Kalberla et al. 2005), and the photon index of the CXB component was fixed at 1.41 (Kushino et al. 2002). Using the formula $apec_{LHB} + wabs \times (apec_{ICM} + apec_{MWH} +$

Table 2. Resultant parameters of the background components.

Cosmic X-ray Background	Local Hot Bubble	Milky-Way halo	
normalization*	normalization [†]	normalization [†]	Reduced- χ^2
	$\times 10^{-3}$	$\times 10^{-4}$	$\chi^2/\text{d.o.f}$
$8.92^{+0.72}_{-0.85}$	$8.93^{+6.02}_{-5.75}$	$1.83^{+1.85}_{-1.72}$	1.04(144/139)

* Measured at 1keV with unit of photons $\text{cm}^{-2} \text{s}^{-1} \text{keV}^{-1} \text{sr}^{-1}$.

[†] Normalization of the APEC component divided by the solid angle, Ω^{U} , assumed in the uniform-sky ARF calculation (20' radius), $Norm = \int n_e n_H dV / (4\pi(1+z)^2 D_A^2) / \Omega^{\text{U}} \times 10^{-14} \text{ cm}^{-5} 400\pi \text{ arcmin}^{-2}$, where D_A is the angular distance to the source.

power-law_{CXB}), we fitted the spectra with a sum of the background components and a single-temperature APEC model for the ICM. Temperature and normalization of the ICM component were allowed to vary, and redshift was fixed at 0.0539. Normalizations of the background components were also left free. The spectra of the filament and void fields were fitted simultaneously, and each parameter of background and abundance of the ICM was assumed to be the same.

Results of the spectral fit are shown in Figure 2. The resulting parameters for the background and ICM are shown in Table 2 and 3, respectively. The normalizations obtained for the CXB and the Galactic components are consistent with those derived by Kushino et al. (2002) and Yoshino et al. (2009), respectively.

Several blank fields observed with Suzaku contained emission with $kT = 0.6 - 0.8 \text{ keV}$ (Yoshino et al. 2009). Therefore, we added an APEC component with $kT = 0.6 \text{ keV}$ and refitted the outermost spectra. The normalization of the 0.6 keV component had a much smaller value than the other Galactic components, and the temperatures and normalizations of the ICM did not change.

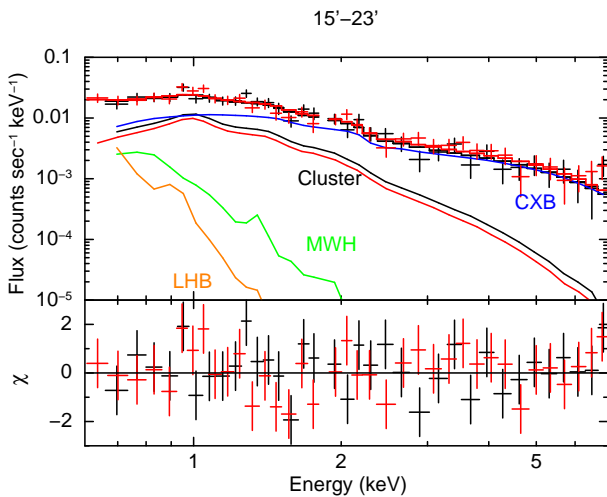


Fig. 2. NXB-subtracted spectra of XIS1 (crosses) for the outermost ring (15'–23' region), fitted by the $apec_{\text{LHB}} + wabs \times (apec_{\text{ICM}} + apec_{\text{MWH}} + \text{power-law}_{\text{CXB}})$ model (stepped solid lines). Black and red colors correspond to the directions in the filament and void, respectively. The bottom panel shows residuals of the fit. The contributions of the ICM are plotted as black and red solid lines, those of the Galactic emission as orange and green lines, and those of the CXB as blue lines.

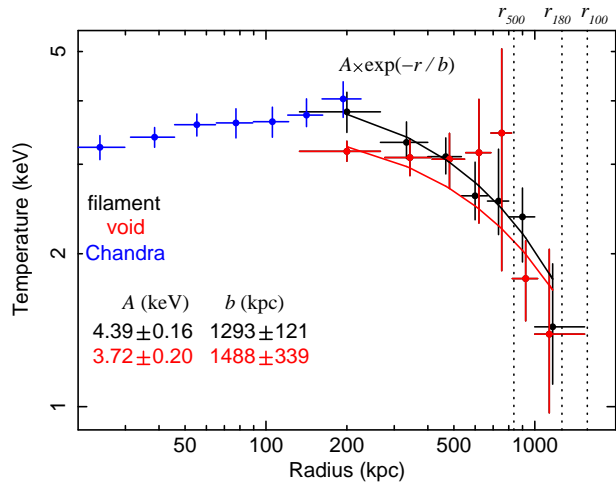


Fig. 4. Radial temperature profiles of the filament (black) and void (red) directions. Solid lines show the best fit function of $A \times \exp(-r/b)$. Chandra results (David et al. 2001) are plotted in blue. Vertical dotted lines show r_{500} , r_{180} , and r_{100} , derived from the fitting of the hydrostatic mass with the NFW universal mass profile (Navarro et al. 1997), as described in subsection 4.4.

3.2. Spectral fits of annular regions

We fitted the XIS spectra in each region of the Hydra A cluster using a single-temperature APEC model for the ICM with the Galactic absorption, N_{H} . The spectra of each annular region of the two fields were fitted simultaneously by minimizing the total χ^2 value. Here, the common background model was included for all regions, where the surface brightness of the background components were restricted within the statistical errors derived for the outermost regions. The temperature and normalization of the ICM component were free parameters. The abundances in each annular region in the two fields were assumed to have the same value. N_{H} was fixed to the Galactic value of $4.7 \times 10^{20} \text{ cm}^{-2}$ in the direction of the Hydra A cluster.

The resultant parameters are summarized in Table 3, and the best-fit spectra are shown in Figure 3. The spectra are well represented with the single-temperature model for the ICM and the background.

4. Results

4.1. Temperature profile

Figure 4 shows the radial temperature profiles of the two directions derived from the spectral fits. At a given radius, the temperatures for each direction are consistent within statisti-

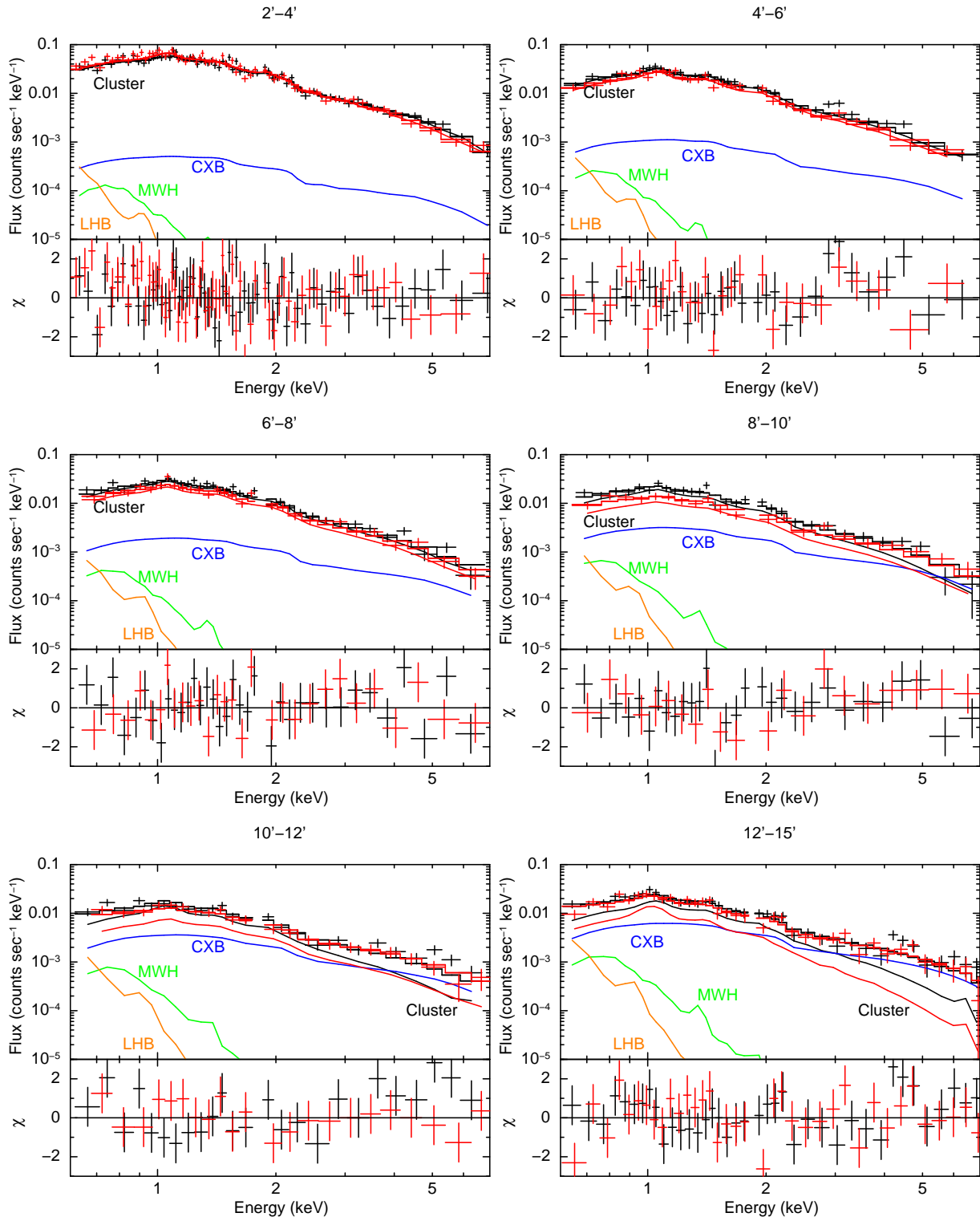


Fig. 3. NXB-subtracted XIS1 spectra fitted with the single temperature (APEC) model for the ICM. Black and red colors correspond to directions toward the filament and void, respectively. Lower panels in each diagram show residual of fit. The contributions of the ICM are plotted as red and black solid lines, while those of the galactic emission and the CXB are plotted as orange, green and blue lines, respectively.

Table 3. Parameters resulting from fitting ICM with the single-temperature APEC model in the energy ranges of 0.7–7.0 keV.

Region		filament			void		
(arcmin)	(kpc)	kT (keV)	abundance (solar)	normalization*	kT (keV)	normalization*	$\chi^2/\text{d.o.f.}$
2' – 4'	133 – 266	$3.81^{+0.35}_{-0.34}$	0.33 ± 0.10	$0.45^{+0.02}_{-0.02}$	$3.18^{+0.15}_{-0.14}$	$0.36^{+0.02}_{-0.02}$	1.22(263/216)
4' – 6'	266 – 400	$3.31^{+0.32}_{-0.23}$	0.43 ± 0.43	$0.10^{+0.01}_{-0.01}$	$3.09^{+0.27}_{-0.24}$	$0.090^{+0.01}_{-0.01}$	1.09(146/134)
6' – 8'	400 – 533	$3.11^{+0.28}_{-0.23}$	0.28 ± 0.15	$0.056^{+0.004}_{-0.005}$	$3.07^{+0.38}_{-0.31}$	$0.035^{+0.003}_{-0.003}$	1.18(177/150)
8' – 10'	533 – 666	$2.60^{+0.43}_{-0.27}$	0.18 ± 0.13	$0.025^{+0.003}_{-0.003}$	$3.16^{+0.86}_{-0.81}$	$0.015^{+0.003}_{-0.002}$	1.18(129/109)
10' – 12'	666 – 799	$2.54^{+0.67}_{-0.36}$	0.38 ± 0.38	$0.013^{+0.003}_{-0.002}$	$3.46^{+1.60}_{-1.60}$	$0.0058^{+0.0016}_{-0.0012}$	1.07(99/93)
12' – 15'	799 – 997	$2.36^{+0.33}_{-0.44}$	0.30 ± 0.19	$0.010^{+0.001}_{-0.001}$	$1.79^{+0.33}_{-0.31}$	$0.0048^{+0.0012}_{-0.0012}$	1.13(170/150)
15' – 23'	997 – 1529	$1.44^{+0.47}_{-0.33}$	0.10 ± 0.08	$0.0036^{+0.0012}_{-0.0011}$	$1.39^{+0.65}_{-0.42}$	$0.0025^{+0.0011}_{-0.0008}$	1.19(263/221)

* Normalization of the APEC, component divided by the solid angle, Ω^U , assumed in the uniform-sky ARF calculation ($20'$ radius), $Norm = \int n_e n_H dV / (4\pi(1+z)^2 D_A^2) / \Omega^U \times 10^{-14} \text{ cm}^{-5} 400\pi \text{ arcmin}^{-2}$, where D_A is the angular distance to the source.

cal errors, except around ~ 200 kpc from the center. The region around 200 kpc corresponds to the shock front detected by Chandra and XMM in the filament direction (Simionescu et al. 2009b; Gitti et al. 2011). From 300 kpc to 1200 kpc, the temperatures in each direction decrease with radius in a similar manner down to ~ 1.4 keV.

From ROSAT observations, Ikebe et al. (1997) found that the spectrum at the central region within $2'$ exhibits the multiphase feature. Although the central $2'$ region was excluded in our spectral analysis, we examined the spectral fits with the two-temperature model in regions with $r > 2'$. The reduced- χ^2 for the two-temperature model was not significantly improved in comparison with the single-temperature model.

To determine the hydrostatic mass of Hydra A, we fitted the temperature profile of each direction with the exponential formula, $A \times \exp(-r/b)$, where A and b are free parameters with units of keV and kpc, respectively, and r is the distance from the X-ray peak of the cluster center. The resulting fit parameters and best-fit functions are shown in Figure 4. In the filament direction, the normalization factor A of the exponential model was 18% higher than that in the void direction, which reflects a temperature difference of ~ 200 kpc. The parameter b for both directions is consistent within statistical error.

4.2. Deprojected electron density profile

We calculated three-dimensional electron density profiles from the normalization of the ICM component derived with Suzaku, considering the geometrical volume that contributes to each two-dimensional region. Here, we assumed spherical symmetry within each direction. The electron density profile was also obtained using XMM data. To avoid uncertainties in the background, we fitted the annular spectra of XMM MOS with the APEC model in an energy range of 1.6–5.0 keV. Here, the temperature and Fe abundance were left free within the error bars derived by Matsushita (2011). We fitted the derived emissivity profiles with a double- β -model, and calculated the three-dimensional radial profile of the electron-density.

Figure 5 shows the electron density profile derived from XMM and Suzaku (this work), Chandra (David et al. 2001) and the ROSAT surface-brightness profile scaled with the XMM density profile at 200 kpc (Ikebe et al. 1997). The deprojected electron density profile derived from XMM and Suzaku observations agree well with those from ROSAT within 500 kpc and from Chandra within 200 kpc.

At a given distance from the X-ray peak, electron density

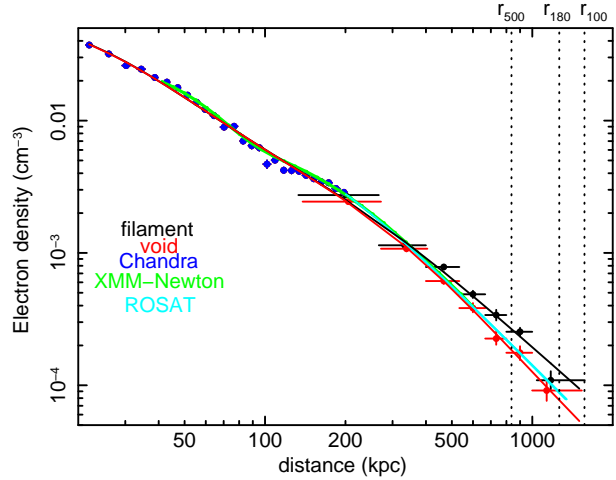


Fig. 5. Deprojected electron density profile of the filament (black) and void (red) directions. Black and red solid lines show the best fit with the double- β model. Green solid line shows the electron density profile derived with XMM data, the light blue solid line shows that derived from the ROSAT surface-brightness profile (Ikebe et al. 1997) scaled with the XMM profile, and the blue filled circles show that derived from Chandra results (David et al. 2001).

beyond 400 kpc in the filament direction was systematically higher than that in the void direction, reflecting the difference in normalizations (Table 3 and Figure 3). At 900 kpc, for example, the deprojected electron densities in the filament and void directions were $(2.54 \pm 0.18) \times 10^{-4} \text{ cm}^{-3}$ and $(1.76 \pm 0.21) \times 10^{-4} \text{ cm}^{-3}$, respectively. The electron density dropped to $\sim 10^{-4} \text{ cm}^{-3}$ around 1200 kpc.

We fitted the density profiles from XMM and Suzaku results with the double- β model from 40 to 1200 kpc. The results are shown in Figure 5, and the resulting parameters are given in Table 4. From 400 kpc to 1530 kpc, the radial profiles of the electron density are also well represented by a power-law profile with slopes of $\Gamma = 1.60 \pm 0.05$ and 1.72 ± 0.07 in the filament and void directions, respectively. The slope of the electron density in the void direction was slightly steeper than that in the filament direction. Fitting the electron density profiles beyond 100 kpc with the single β -model resulted in $\beta = 0.61 \pm 0.02$ and $\beta = 0.74 \pm 0.03$ for the filament and void directions, respectively. These values are close to the value of 0.68 derived from the ROSAT surface-brightness profile (Ikebe et al. 1997).

Table 4. Parameters resulting from fitting the deprojected density profile derived from XMM and Suzaku with the double- β model*.

Field	narrower component			wider component		
	$n_{0,1}$ (10^{-2} cm $^{-3}$)	$r_{c,1}$ (kpc)	β_1	$n_{0,2}$ (10^{-3} cm $^{-3}$)	$r_{c,2}$ (kpc)	β_2
void	6.73 ± 0.17	21.3 ± 4.7	0.59 ± 0.01	2.16 ± 0.14	278 ± 264	0.95 ± 0.07
filament	6.61 ± 0.19	22.3 ± 5.4	0.62 ± 0.01	2.73 ± 0.15	193 ± 114	0.60 ± 0.03

* double- β model is given by the form $n(r) = n_{0,1}(1 + (r/r_{c,1})^2)^{-3\beta_1/2} + n_{0,2}(1 + (r/r_{c,2})^2)^{-3\beta_2/2}$.
The errors of $n_{0,1}$ and β_1 are calculated by fixing the $r_{c,1}$ and wider component, and vice versa.

Table 5. Resultant fit parameters of the deprojected density profile derived from XMM and Suzaku with the single- β model* beyond 100 kpc.

Field	n_0 (10^{-3} cm $^{-3}$)	r_c (kpc)	β
void	7.38 ± 0.42	160 ± 13	0.74 ± 0.03
filament	7.98 ± 0.50	131 ± 10	0.61 ± 0.02

* single- β model is given by the form $n(r) = n_0(1 + (r/r_c)^2)^{-3\beta/2}$.

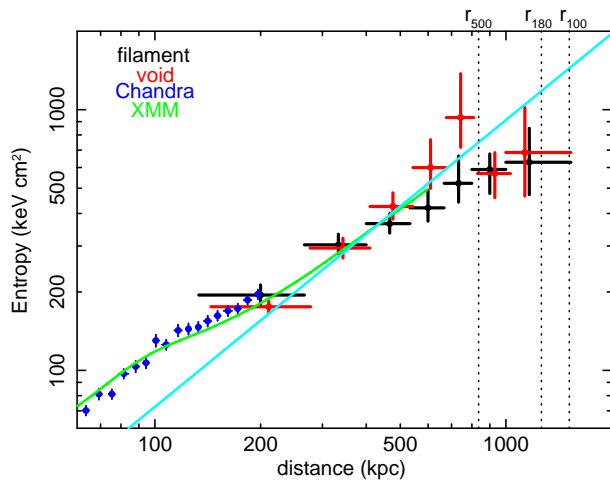


Fig. 6. Entropy profiles in the filament (black) and void (red) directions. Crosses and diamonds show entropy calculated from the resulting temperature and electron density, respectively, as shown in Figures 4 and 5. Chandra results (David et al. 2001) are represented by blue crosses. The green line shows the entropy profile calculated by combining the electron density from XMM and the temperature from Suzaku. The light blue line extrapolates the Suzaku and XMM data (green line) with a power-law formula fit for the data beyond 200 kpc, which has a fixed index of 1.1.

4.3. Entropy profiles

Entropy, which is a useful tool for investigating the thermodynamic history of hot gas in groups and clusters, is defined as

$$S = \frac{kT}{n_e^{2/3}}, \quad (1)$$

where T and n_e are the temperature and deprojected electron density, respectively. In Figure 6, we show the entropy profiles of the Hydra A cluster calculated from the derived temperature and electron density profiles shown in Figures 4 and 5. Entropy in the two directions increased from the center to 800 kpc, or r_{500} , which was derived from the Navarro, Frenk and White(NFW) model fit to the hydrostatic mass described in section 4.4. Between 500 kpc and 800 kpc, the entropy in the void direction was systematically higher than in the filament

direction. At the two outermost radial bins (beyond r_{500}), the entropies of the two directions agree well. In addition, we calculated the entropy profile by combining the parameters resulting from the fit of the electron density profile from XMM and the temperature profile from Suzaku as indicated by the green line in Figure 6. The entropy profiles using Suzaku, XMM, and Chandra data are consistent with each other (figure 6).

The derived entropy profiles were compared with a power-law model with a fixed index of 1.1, which was expected from simulations of the accretion shock heating model (Tozzi & Norman 2001; Ponman, Sanderson, Finoguenov 2003). From 200 kpc to 500 kpc, the derived entropy profiles agreed well with the $r^{1.1}$ relationship. In contrast, beyond 800 kpc, or $\sim r_{500}$, the entropy profiles in the two directions were systematically lower than the predicted by the $r^{1.1}$ relationship. Inside 200 kpc, the entropy exceeded the model prediction, which attribute to the presence of the cool core boundary (Peres et al. 1998) and the shock front around 200 kpc.

4.4. Hydrostatic mass

We estimated the hydrostatic or gravitational mass assuming the hydrostatic equilibrium given by,

$$M_{H.E.}(< r) = -\frac{kT(r)r}{\mu m_p G} \left(\frac{d \ln \rho(r)}{d \ln r} + \frac{d \ln kT(r)}{d \ln r} \right), \quad (2)$$

where $M_{H.E.}(< r)$ is the hydrostatic mass within the three-dimensional radius r , G is the gravitational constant, k is the Boltzmann constant, ρ is the gas density, kT is the temperature, and μm_p is the mean particle mass of the gas (the mean molecular weight is $\mu = 0.62$). Here, we assumed spherically symmetric mass distribution.

On the basis of the temperature and electron density profiles, we calculated the hydrostatic mass of the Hydra A cluster beyond 100 kpc. The temperature gradient of the i th shell was calculated from a power-law fit of temperatures of shells ($i-1$), i , and ($i+1$). We employed the electron density profile from the single- β model fit shown in table 5. The derived hydrostatic mass is plotted in Figure 7 as diamonds with the integrated gas mass profiles and stellar mass profiles derived in subsection 4.6. The derived mass was calculated for the whole azimuthal angle under the assumption of spherical symmetry

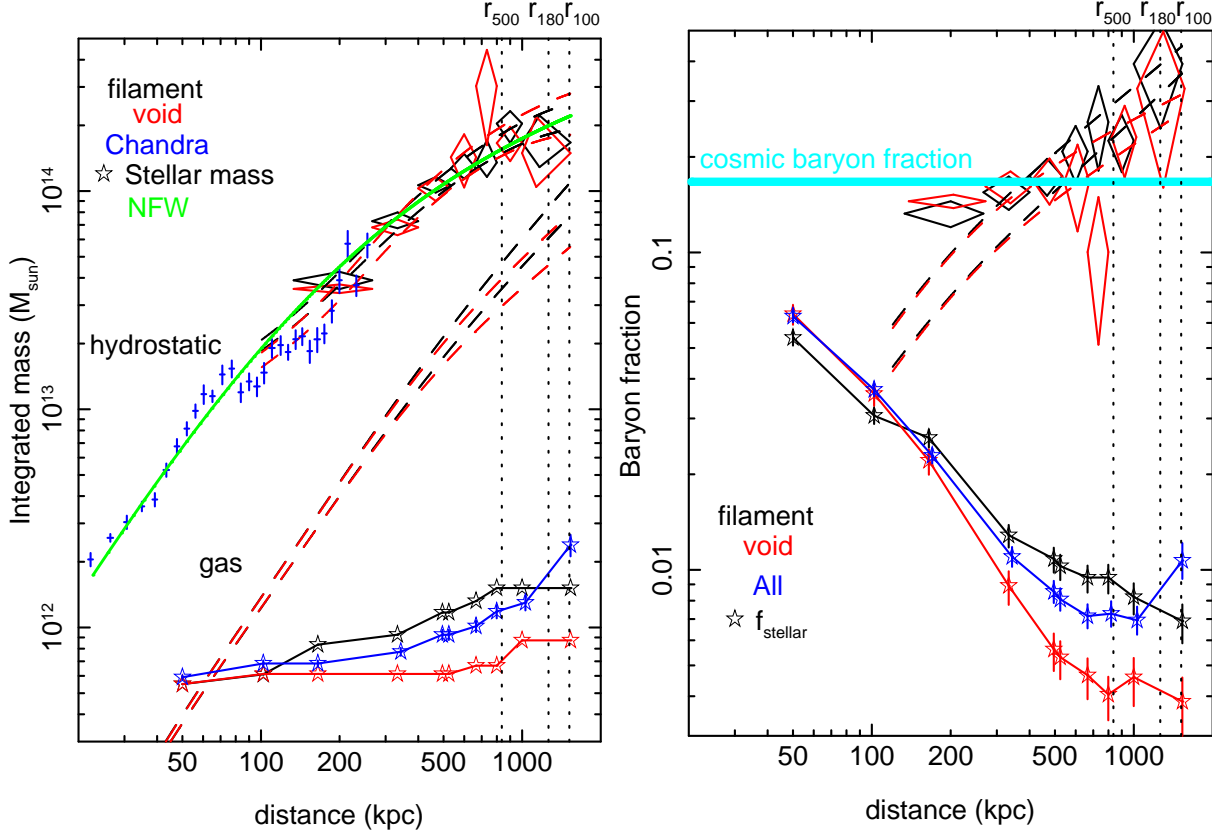


Fig. 7. left: Integrated hydrostatic and gas-mass profiles. All the black and red colors show the filament and void directions, respectively. The masses were calculated in the whole azimuthal angle under the assumption of spherical symmetry for each direction. The hydrostatic mass was calculated from the temperatures of shells ($i - 1$), i , and ($i + 1$) (diamonds) and the exponential relationship (dashed lines). All dashed lines show 90% upper and lower limits. The green line shows the best-fit NFW model. The integrated stellar mass profiles in the filament and void directions using 2MASS data are represented by stars. Blue stars are the integrated stellar mass profile in the whole azimuthal angle corrected for the contribution of the fainter galaxies using LF (solid). right: Cumulative profiles of gas fraction, $f_{\text{gas}}(< r)$ assuming hydrostatic equilibrium in both directions. The diamonds show $f_{\text{gas}}(< r)$ of the integrated hydrostatic and gas mass of the corresponding directions. Dashed lines represent $f_{\text{gas}}(< r)$ applying the result of the NFW model fit. The value of the cosmic baryon fraction (light blue) from WMAP (Komatsu et al. 2011) is plotted. The stars represent the stellar fraction, $f_{\text{star}}(< r)$, using the NFW model fit. The meanings of the colors and line styles are the same as in the left panel.

using the parameters derived for each direction: thus, the mass in each direction was four times larger than that in the corresponding direction. Although the electron density in the filament direction at a given radius was higher than that in the void direction, the difference in the slopes of the electron density was small. As a result, the hydrostatic masses derived for the two directions agree well. In addition, we calculated the 90% range of hydrostatic mass using the exponential relationship of the temperature profiles and fits of the electron-density profiles with the double- β model, which are plotted as dashed lines in Figure 7.

We fitted the derived hydrostatic mass profiles with the following NFW formula, which shows the equilibrium density profile of the dark matter halo (Navarro et al. 1996; Navarro et al. 1997);

$$M_{\text{NFW}}(< r) = 4\pi\delta_c\rho_c r_s^3 \left[\ln(1+x) - \frac{x}{1+x} \right], x \equiv r/r_s, (3)$$

where $M_{\text{NFW}}(< r)$ is the mass within a radius r , ρ_c is the critical baryon density of the Universe, r_s is the scaled radius, and δ_c is the characteristic density, that can be expressed in terms of the concentration parameter ($c = r_{200}/r_s$) as

$$\delta_c = \frac{200}{3} \frac{c^3}{\ln(1+c) - c/1+c}. (4)$$

Since the hydrostatic masses derived for the two directions agree well, we fitted the two hydrostatic mass profiles with Suzaku and that with Chandra simultaneously, excluding the shock region from 100 kpc to 200 kpc. The parameters derived from the fit are shown in Table 7. The quantity r_{100} is equal to r_{vir} in Hydra A cluster, since for our fiducial cosmological model, $\Delta_{\text{vir}} = 100$ for halos with a redshift $z = 0.0539$ (Nakamura & Suto 1997). We estimated r_{Δ} for various overdensities: $\Delta = 500, 200, 180$ and 100 , and r_{Δ} derived from fits with the NFW model are 811 ± 10 kpc, 1189 ± 96 kpc, 1243 ± 16 kpc, and 1577 ± 22 kpc, respectively. The r_{100} is close to the outermost ring radius. Possible deviations from hydrostatic equilibrium have been previously discussed to explain the entropy flattening beyond r_{500} (Bautz et al. 2009; George et al. 2009; Kawaharada et al. 2010): therefore, we fitted the hydrostatic mass out to r_{500} . We were able to obtain almost the same results as shown in Table 7. Thus, the NFW model represents the hydrostatic mass out to r_{100} within error bars as shown in Figure 7.

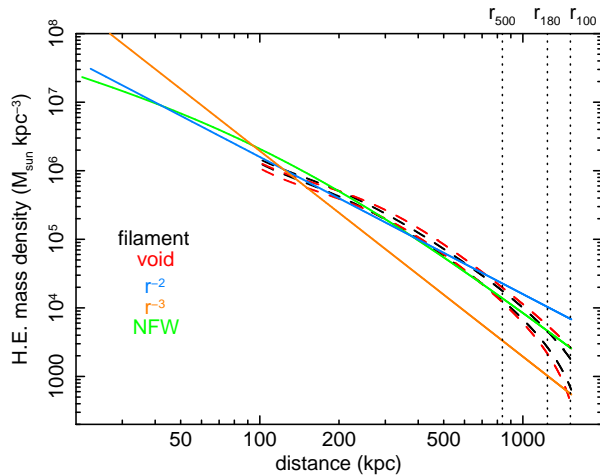


Fig. 8. H.E. mass density profiles for the filament (black) and void (red) directions. Density was calculated from the integrated H.E. mass profile. The r^{-2} and r^{-3} profiles are plotted with solid blue and orange lines, respectively.

Moreover, we calculated the total mass density profile from the total integrated hydrostatic mass profile in each direction. The density profile was also calculated from the NFW model obtained above. The calculated density profiles were compared with r^{-2} and r^{-3} profiles (Figure 8). The NFW density profile varied from r^{-1} to r^{-3} with increasing radius. Within r_{500} , the densities are well represented by the r^{-2} profile, which is shallower than the asymptotic matter density slope $\rho \propto r^{-3}$. Beyond r_{500} , the r^{-3} profile is preferable than the r^{-2} profile.

4.5. Gas fraction

We derived the cumulative gas mass fraction as,

$$f_{\text{gas}}(< r) = \frac{M_{\text{gas}}(< r)}{M_{\text{H.E.}}(< r)}, \quad (5)$$

where $M_{\text{gas}}(< r)$ and $M_{\text{H.E.}}(< r)$ are the gas mass and hydrostatic mass, respectively, within a sphere of radius r . As shown in Figure 7 and Table 6, the gas fraction increased in the outskirts and reached the cosmic mean baryon fraction derived from seven-year data of Wilkinson microwave anisotropy probe (WMAP7; Komatsu et al. 2011) at $\sim 0.5 r_{500}$. At r_{100} , $f_{\text{gas}}(< r)$ in the filament direction exceeded the result of WMAP7, while the lower limit of $f_{\text{gas}}(< r)$ in the void direction reached the WMAP 7 fraction. Adopting the fit of the NFW model to the hydrostatic mass resulted in $f_{\text{gas}}(< r)$ in the void and the filament directions at r_{100} , exceeding the cosmic baryon fraction by a factor of 2 and 3, respectively. Furthermore, $f_{\text{gas}}(< r)$ in the void direction at r_{180} was close to that derived for the north-west direction of the Perseus cluster at r_{200} (Simionescu et al. 2011): r_{180} was derived from the NFW model fit of the hydrostatic mass. The radial profile of $f_{\text{gas}}(< r)$ of the Abell 1246 cluster with $kT = 6.0$ keV exhibited similar behavior as that of our result of the Hydra A cluster (Sato et al. 2012).

4.6. K-band Luminosity of galaxies and stellar fraction

The ratio of gas mass to stellar luminosity is a key parameter for studying the star formation efficiency in clusters

of galaxies. Since almost all metals in the ICM are synthesized in galaxies, the metal-mass-to-light ratio provides a useful measure for studying the ICM chemical evolution. To estimate the gas-mass and Fe-mass-to-light ratios, we calculated the K -band luminosity of Hydra A cluster on the basis of the Two Micron All Sky Survey (2MASS) catalog, whereby all data is presented in a $2^\circ \times 2^\circ$ box: the coordinates of objects are shown in the left panel of Figure 9. The smoothed distribution of galaxies around Hydra A obtained from 2MASS is shown in the right panel of Figure 9. The distribution of galaxies is elongated in the filament direction toward the Abell 754 cluster, which exhibited a redshift close to that of Hydra A. In the void direction, the density of galaxies was significantly lower. Toward the south, an additional filament-like distribution of galaxies appeared from the Hydra A cluster. Hydra A itself was discovered to have an apparent magnitude of $m_K = 11.07$, or $L_K = 5 \times 10^{11} L_{K,\odot}$ using a luminosity distance $D_L = 240$ Mpc and a foreground Galactic extinction of $A_K = 0.015$ (Schlegel, Finkbeiner, Davis 1998). Among galaxies in the NED data base² with available redshifts, those with heliocentric velocities differ from that of the Hydra A cluster by >2000 km/s were excluded from the analysis. The K -band surface brightness profile centered on Hydra A is shown in figure 10. Beyond ~ 2000 kpc from the cluster center, the K -band surface brightness flattened. Therefore, we adopted the region between 2000 kpc and 4000 kpc as a background.

Figure 10 also shows the luminosity function (LF) of galaxies in the Hydra A cluster within r_{100} . Here, we used as background the LF of galaxies from 2000 kpc to 4000 kpc from the center of the Hydra A cluster. The completeness limit of galaxies of 2MASS is $K_s = 13.5$ in apparent magnitude³, which corresponds to the K -band luminosity, $L_K = 7 \times 10^{10} L_{K,\odot}$ for the distance of the Hydra A cluster. The total K -band luminosity of galaxies above the 2MASS complete limit and that of all the detected galaxies including those below the limit are $1.5 \times 10^{12} L_{K,\odot}$ and $2.5 \times 10^{12} L_{K,\odot}$, respectively. To calculate the total light of the cluster, we evaluate the contribution of fainter galaxies below the 2MASS limit. The LF of galaxies in clusters can be described with the Schechter function as,

$$\phi(L)dL = \phi_* \left(\frac{L}{L_*}\right)^\alpha \exp(-L/L_*) d\left(\frac{L}{L_*}\right) \quad (6)$$

where the parameters L_* , ϕ_* , and α are the characteristic luminosity, number densities, and faint-end power-law index, respectively. Upon adopting the L_* of stacked cluster galaxies by Lin, Mohr, Stanford (2003) and integrating the Schechter function below the 2MASS limit, the total K -band luminosity becomes $2.2 \times 10^{12} L_{K,\odot}$, which is smaller than that of all the galaxies detected by 2MASS including those below the complete limit. If we allow L_* to vary, the fit for the LF of the Hydra A cluster improves, as shown in Figure 10, and the total K -band luminosity becomes $2.8 \times 10^{12} L_{K,\odot}$. Therefore, the simple sum of K -band luminosities of the detected galaxies, including those below the 2MASS complete limit is close to that integrated luminosity of the Schechter function. Therefore, we adopted the total K -band luminosity

² <http://nedwww.ipac.caltech.edu/>

³ See <http://www.ipac.caltech.edu/2mass/releases/second/doc/explsum.html>

Table 6. Cumulative values of the hydrostatic mass ($M_{H.E.}$), gas mass (M_{gas}), and gas fraction (f_{gas}) of the Hydra Hydra A cluster.

Region r (kpc)	filament			void		
	M_{gas} ($10^{14} M_{\odot}$)	$M_{H.E.}$ ($10^{14} M_{\odot}$)	f_{gas}	M_{gas} ($10^{14} M_{\odot}$)	$M_{H.E.}$ ($10^{14} M_{\odot}$)	f_{gas}
133 – 266	0.052 ± 0.001	0.39 ± 0.04	0.13 ± 0.01	0.052 ± 0.001	0.36 ± 0.02	0.15 ± 0.01
266 – 400	0.11 ± 0.01	0.72 ± 0.07	0.15 ± 0.02	0.11 ± 0.01	0.68 ± 0.06	0.16 ± 0.02
400 – 533	0.19 ± 0.02	1.06 ± 0.09	0.17 ± 0.02	0.17 ± 0.02	1.03 ± 0.13	0.17 ± 0.03
533 – 666	0.26 ± 0.03	1.27 ± 0.21	0.21 ± 0.04	0.24 ± 0.03	1.43 ± 0.39	0.17 ± 0.05
666 – 799	0.35 ± 0.05	1.35 ± 0.35	0.26 ± 0.08	0.30 ± 0.04	3.03 ± 1.41	0.10 ± 0.05
799 – 997	0.46 ± 0.07	2.04 ± 0.37	0.22 ± 0.05	0.38 ± 0.06	1.66 ± 0.31	0.23 ± 0.06
997 – 1529	0.71 ± 0.12	1.82 ± 0.60	0.39 ± 0.14	0.55 ± 0.11	1.67 ± 0.78	0.33 ± 0.17

Table 7. Resulting radii r_c and r_{200} , and concentration parameter c_{200} derived from the NFW model.

	r_s (kpc)	r_{200} (kpc)	c
fitted up to r_{500}	126 ± 8	1189 ± 96	9.44 ± 0.48
fitted up to r_{100}	123 ± 8	1183 ± 98	9.62 ± 0.49

of $(2.5 \pm 0.3) \times 10^{12} L_{K,\odot}$.

We collected K -band luminosity of galaxies in the north-west and north-east sectors for the filament and void directions, respectively, as well as in the whole azimuthal angle and derived brightness profiles in the K -band. For the whole azimuthal angle, we collected galaxies above the 2MASS complete limit and evaluated the contribution of fainter galaxies by integrating the Schechter function. We obtained almost the same radial profile of K -band luminosity as that from the simple sum of luminosities of all the galaxies detected with 2MASS. Therefore, for the filament and void directions, we collected all the galaxies detected by 2MASS in each direction and derived radial profile of K -band luminosity. After subtracting the background, we deprojected the brightness profile of galaxies (under the assumption of spherical symmetry) and derived three-dimensional radial profiles of K -band luminosity in the filament, void, and whole azimuthal angle.

Figure 7 shows the integrated K -band luminosity profiles. As opposed to the integrated luminosity of the whole azimuthal angle, figure 7 uses the four-times luminosity of the filament and void directions. The filament direction shows a systematically higher K -band luminosity than that in void direction. The integrated K -band luminosity profiles of these two directions become flatter from ~ 800 -1000 kpc, and the contribution of galaxies beyond 1000 kpc is small. The integrated luminosity profile of the whole azimuthal angle is between those in the filament and void directions except for the outermost region around 1200 kpc (Figure 7 and 9). This result is attributed to the luminosity of the whole azimuthal angle being affected by the filamentary structure around 1200 kpc in the south of the Hydra-A cluster.

We derived cumulative stellar mass fraction as,

$$f_{\text{star}}(< r) = \frac{M_{\text{star}}(< r)}{M_{\text{H.E.}}(< r)} \quad (7)$$

where, $M_{\text{star}}(< r)$ is the total stellar mass within r , derived from the total K -band luminosity within r , under the assumption that the stellar-mass-to-light ratio in the K -band is unity (Nagino & Matsushita 2009). At a given radius, the $f_{\text{star}}(< r)$

in the filament direction is higher by a factor of 2–3 than that in the void direction, reflecting the concentration of galaxies in the filament direction (Figure 7). Beyond r_{500} , $f_{\text{star}}(< r)$ is smaller than $\sim 1\%$, and does not contribute to the baryon fraction. We also derived the stellar mass fraction using the whole azimuthal angle using the NFW mass for the filament and void directions. Although the stellar fraction continues to decrease with radius in the filament and the void directions, the stellar fraction in whole azimuthal directions shows a minimum at $\sim r_{500}$, and increases with radius by a factor of ~ 1.5 from r_{500} to r_{100} .

Using the integrated K -band luminosity profile, we calculated the gas-mass-to-light ratio in the filament and void directions (Figure 11). The radial profile of the gas-mass-to-light ratio in the two directions increased with radius out to r_{100} . We also calculated the gas-mass-to-light ratio in the whole azimuthal angle, using the stellar luminosity in the whole azimuthal angle and the gas mass in the void direction which agrees that for the whole azimuthal angle derived by ROSAT (Ikebe et al. 1997).

5. Discussions

The Hydra A cluster is the first medium-sized cluster observed with Suzaku out to the virial radius. Suzaku observed the northern half of the cluster, and we derived radial profiles of temperature, electron density, entropy, hydrostatic mass, and K -band stellar luminosity in the filament and void directions. Temperature and entropy carry important information about the thermal history of the ICM. In subsection 5.1, we compare these profiles of the Hydra A cluster and other clusters observed with Suzaku and XMM to study their dependence on the system mass or on average ICM temperature. Next, we discuss possible explanations for entropy flattening and the higher gas-mass-to-hydrostatic-mass ratio at cluster outskirts. Discrepancies between electron and ion temperatures are discussed in subsection 5.2, deviations from hydrostatic equilibrium and the gas-clumping effect are discussed in subsections 5.3 and 5.4. We also derive IMLR of the Hydra A cluster out

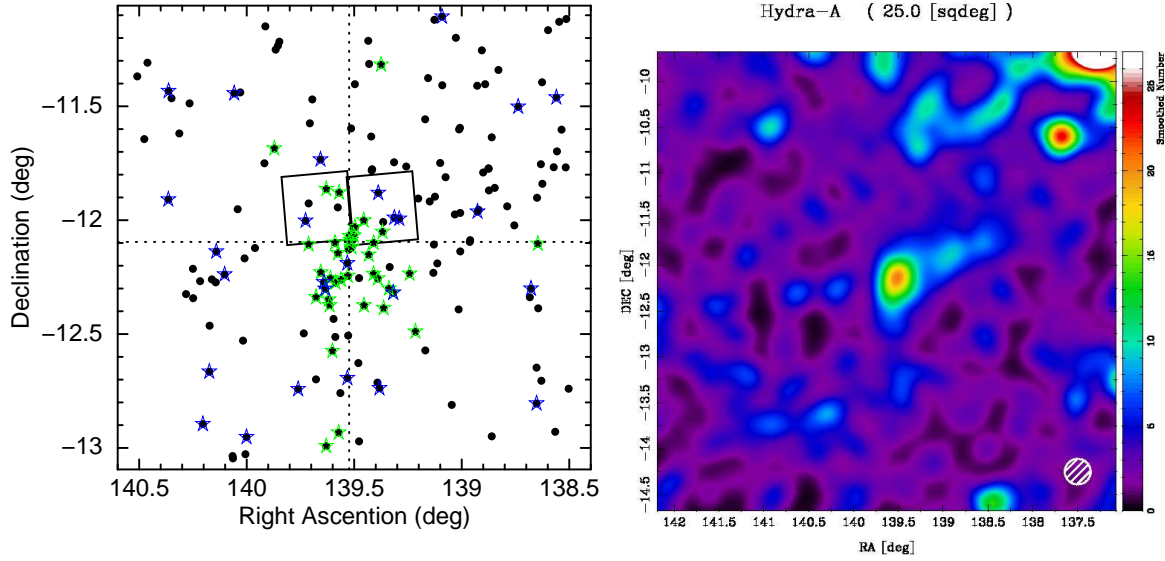


Fig. 9. Two-dimensional density distributions of galaxies around Hydra A, retrieved from 2MASS in the K -band. left: Stars represent galaxies with available redshift in the NASA/IPAC Extragalactic Database (NED). Green and blue stars indicate members and non-members, respectively, of the Hydra A cluster based on their redshift. The boxes represent the Suzaku fields of view (FOVs) of XIS pointings. The directions of the filament (north-west) and the void (north-east) are separated as dashed lines. Right: The box size is $5^\circ \times 5^\circ$. Abell 754 cluster, with coordinates (RA, Dec) = (137.2087, -9.6366) in degrees, is shown in top right. A Gaussian smoothing scale is represented by the white hatched circle at bottom right.

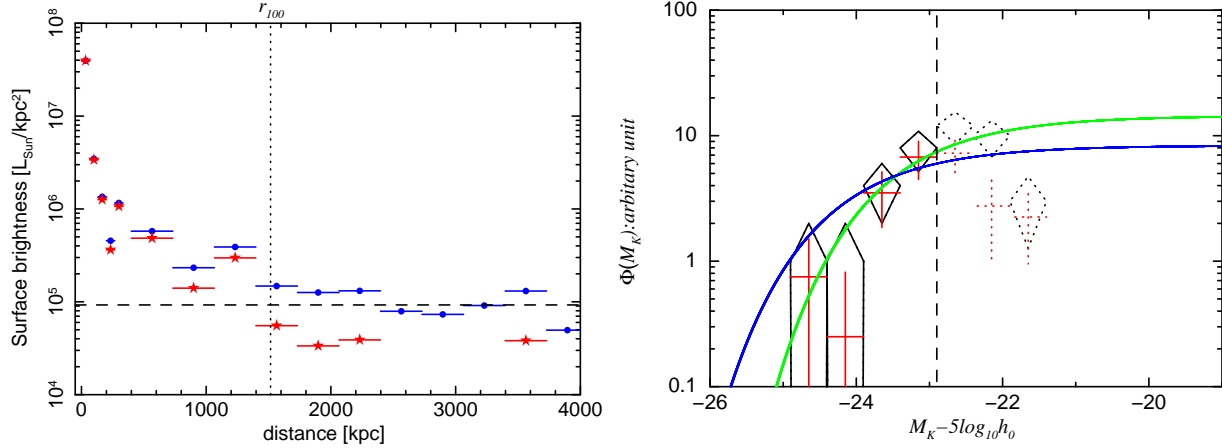


Fig. 10. left: Surface-brightness profile of Hydra A observed with 2MASS photometric data in the K -band. Blue points denote the detected galaxies of Hydra A and red stars denote the background-subtracted data. The dashed line shows the subtracted background level and the dotted line shows r_{100} . right: The LF of Hydra A observed with 2MASS photometric data in the K -band within r_{100} in absolute magnitude form, including background galaxies (black diamonds) and that the subtracted background contribution (red crosses). The vertical dashed line represents the complete limit of 2MASS. Blue dashed line and green solid line show the best-fit Schechter functions when L_* was fixed to the result from the stacked LF of galaxies in clusters by Lin, Mohr, Stanford (2003) and allowed to vary, respectively.

to the virial radius in subsection 5.5 to constrain the star formation history in the cluster.

5.1. Comparison of temperature and entropy profiles with other systems

Figure 12 compares the temperature profiles of the Hydra A cluster and several clusters observed with Suzaku, scaled with average temperature, $\langle kT \rangle$, and r_{200} . Here, $r_{200} = 2.77 h_{70}^{-1} \sqrt{\langle kT \rangle / 10 \text{ keV}} / E(z)$ Mpc, with $E(z) = (\Omega_M(1+z)^3 + 1 - \Omega_M)^{1/2}$ (Henry et al. 2009). Then, r_{200} of the Hydra A cluster is 1.48 Mpc. Within $0.5r_{200}$, the temperature profiles agree with the scaled temperature relationship by Pratt et al.

(2007), which is derived from a sample of 15 clusters observed with XMM out to $\sim r_{500}$. In contrast, beyond $0.5r_{200}$, the observed temperatures scatter by a factor of two, and tend to be lower than the XMM relationship. In the scaled temperature profiles, there was no evidence of any significant dependence on the average ICM temperature, or system mass. Some variation in the temperature profiles should reflect the azimuthal variation as observed in Abell 1689 (Kawaharada et al. 2010) and Abell 1246 (Sato et al. 2012).

In figure 13, we compare the entropy profile of the Hydra A cluster with other clusters observed with Suzaku; these profiles are scaled with the average ICM temperature and r_{200} by

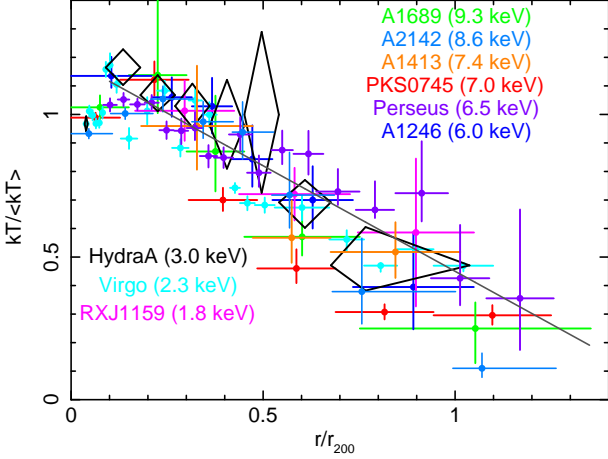


Fig. 11. Cumulative gas-mass-to-light ratio M_{gas}/L_K in the filament (black) and void (red) directions and for the whole azimuthal angle (blue).

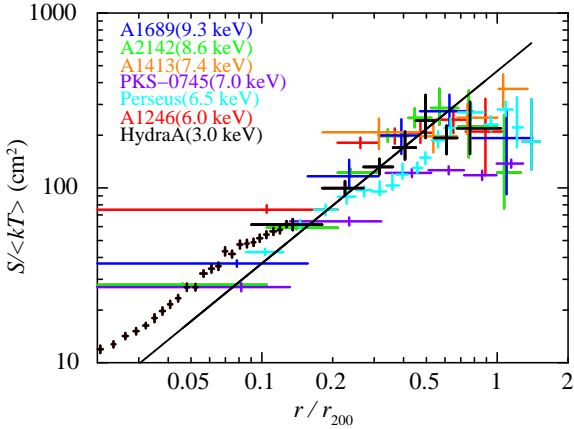


Fig. 12. Radial profiles of temperature of clusters observed with Suzaku and XMM. Here, the temperature profiles are scaled with the average ICM temperature, $\langle kT \rangle$, and are azimuthally averaged. We plotted the radial profiles of cluster of galaxies Abell 1689 (Kawaharada et al. 2010), Abell 2142 (Akamatsu et al. 2011), Abell 1413 (Hoshino et al. 2010), PKS-0745 (George et al. 2009), the Perseus cluster (Simionescu et al. 2011), Abell 1246 (Sato et al. 2012), the Virgo cluster (Urban et al. 2011), RXJ1159 (Humphrey et al. 2011) and the Hydra A cluster (current study). The scaling radius r_{200} was calculated by Henry et al. (2009). The solid line represents the scaled temperature profile by Pratt et al. (2007).

Henry et al. (2009). Here, we used the weighted average of the radial profiles of different directions of each cluster. Contrary to the expected $r^{1.1}$ relationship, these profiles become flat beyond $0.5r_{200}$. Except for PKS-0745 (George et al. 2009), the scaled entropy profiles of these clusters were universal with ICM temperatures above 3 keV and did not depend on the ICM temperature. For the PKS-0745 cluster, Eckert et al. (2011) determined that the ROSAT surface-brightness profile is statistically inconsistent (7.7σ) with Suzaku results beyond r_{200} and that the difference is likely explained by the existence of additional foreground components at the low Galactic latitude of the source. These components were not considered in the Suzaku background modeling.

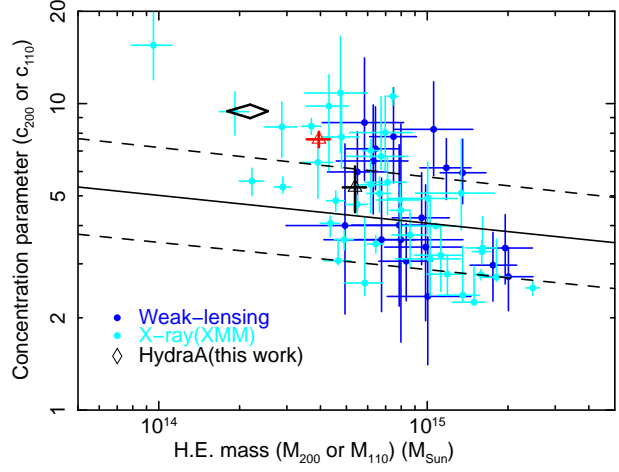


Fig. 13. Radial profiles of entropy of cluster observed with Suzaku and scaled: with the average ICM temperature, $\langle kT \rangle$, and are azimuthally averaged. Data for Abell 1689 (Kawaharada et al. 2010) are plotted in dark blue, for Abell 2142 (Akamatsu et al. 2011) in green, for Abell 1413 (Hoshino et al. 2010) in orange, for PKS-0745 (George et al. 2009) in purple, for Perseus (Simionescu et al. 2011) in light blue, for Abell 1246 (Sato et al. 2012) in red, and for Hydra A (current study) in black. The scaling radius r_{200} was calculated by Henry et al. (2009). The solid line shows the power-law profile with slope of 1.1. The normalization of the power-law is scaled with our result for the Hydra A cluster.

5.2. Ion-electron relaxation in the Hydra A cluster

One interpretation for the flattening of the entropy profile is that caused by deviations in electron and ion temperatures (Hoshino et al. 2010; Akamatsu et al. 2011). The time-scale for thermal equilibration between electrons and ions through Coulomb scattering is given by

$$t_{ei} \sim 0.14 \left(\frac{n_e}{10^{-4} \text{ cm}^{-3}} \right)^{-1} \left(\frac{kT}{1.5 \text{ keV}} \right)^{3/2} \text{ Gyr} \quad (8)$$

(Takizawa & Mineshige 1998; Takizawa 1998; Takizawa 1999; Akahori & Yoshikawa 2010). Considering this time-scale and the shock propagation speed, the radial length above which the electron temperature is significantly lower than the ion temperature is proportional to the square of the ICM temperature (Takizawa 1999). On the other hand, r_{200} is proportional to the square root of the ICM temperature. Therefore, some dependence on the mean ICM temperature is expected in the temperature and entropy profiles. However, there is no systematic dependence on the average ICM temperature in the temperature and entropy profiles, as shown in figure 12 and figure 13. Furthermore, if the ICM temperature is underestimated and the actual entropy profile of the Hydra A cluster follows the $r^{1.1}$ relationship, a flat ICM temperature profile is necessary, i.e., $r \sim 0$ out to r_{100} , considering the electron density profile of $r^{-(1.6 \sim 1.7)}$ beyond 400 kpc. However, the flat temperature profile contradicts to the results of numerical hydrodynamical simulations, where negative gradients of the temperature profiles outside cool core regions are naturally produced (Borgani et al. 2002; Burns et al. 2010; Nagai & Lau 2011). Therefore, for the Hydra A cluster, it is difficult to explain the flattening of the observed entropy profiles by deviations of ion-electron

temperatures.

5.3. Deviations from hydrostatic equilibrium

The remaining interpretation for the flattening of the entropy profiles at the cluster outskirts is deviations from hydrostatic equilibrium, because when the gas-clumping effect is significant, we also expect that the ICM also deviates from hydrostatic equilibrium. Then, infalling matter may have retained some of its kinetic energy in the form of bulk motions, and the thermal energy deficit in the ICM yields lower entropy. Furthermore, the underestimate of the gravitational mass and/or gas clumping leads to an overestimation of the baryon fraction. Recent numerical simulations by Vazza et al. (2009) and Nagai, Vikhlinin, Kravtsov (2007) have shown that the kinetic energy of bulk motion carries $\sim 30\%$ of the total energy around the virial radius. With simulations, Nagai & Lau (2011) showed that beyond r_{200} , gas clumping leads to an overestimation of the observed gas density and causes flattening of the entropy profile. If the hydrostatic mass was underestimated by 130% in the filament direction and 100% in the void direction, the baryon fractions at r_{100} would have the same value as that of WMAP7, although the observed gas fraction calculated from the hydrostatic mass in the void direction is consistent with the WMAP7 result within error bars.

The distributions of the ICM and galaxies in the Hydra A cluster elongate in the filament direction. If the ICM is under hydrostatic equilibrium in a non-spherical dark matter halo, the X-ray emission and dark matter halo elongate in the same direction. Numerical simulations by Burns et al. (2010) determined that gas, galaxies, and dark matter continue in the filament direction due to the accretion of gas and subclusters. Then, it is reasonable that the dark matter halo also elongates in the filament direction. However, the hydrostatic mass in the void and filament directions of the Hydra A cluster are in good agreement. These results indicate that deviations from hydrostatic equilibrium should be more significant in the filament direction than in the void direction.

The clumping effect will also be higher in the filament direction, since smaller systems are thought to be accreted from this direction. For the Hydra A cluster, we were not able to detect clump candidates with Suzaku. The spectra of detected point sources are consistent with those of background active galactic nuclei. Considering the luminosities of detected point sources, the luminosity of clumps should be smaller than a few 10^{41} erg s^{-1} , which corresponds to cores of groups of galaxies. Therefore, if clumps are significant, their scales should be smaller than those of small groups of galaxies.

5.4. The concentration-mass relationship

From numerical simulations, a weak variation in the concentration is expected from low-mass to high-mass clusters, reflecting differences in the formation epochs of low-mass and high-mass halos (Navarro et al. 1997; Bullock et al. 2001; Dolag et al. 2004). Pointecouteau, Arnaud, Pratt (2005), Ettori et al. (2011) and Okabe et al. (2010) investigated the relationship between the concentration parameter and the cluster mass, or the concentration-mass ($c - M$) relationship. The results are compatible with the intrinsic dispersion of theoretical predictions. Figure 14 compares the $c - M$ relationship of the

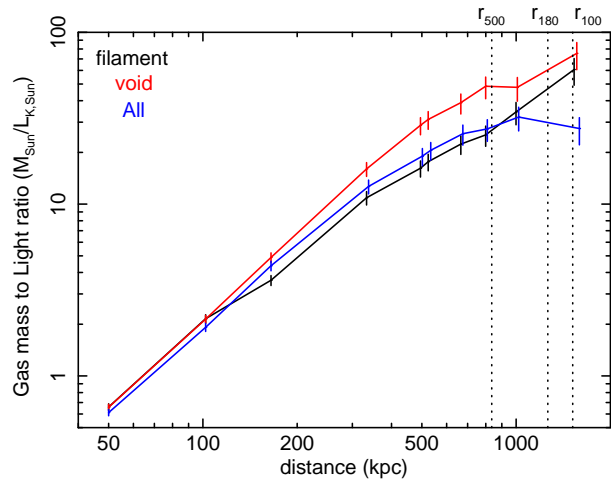


Fig. 14. Observed distribution of concentration parameters as a function of cluster masses. The mass of weak lensing (blue) and X-ray (light blue) were defined by Okabe et al. (2010) and Ettori et al. (2010);Ettori et al. (2011), respectively. Okabe et al. (2010) used M_{110} and c_{110} , while Ettori et al. (2010);Ettori et al. (2011) used M_{200} and c_{200} . We considered M_{100} for Hydra A. The solid line indicates the median relationship determined through CDM simulations for the WMAP5 cosmological model, while the region enclosed within the dashed lines corresponds to the range of $\sigma(\log_{10} c) = 0.1$, within which most of simulated clusters are distributed (Duffy et al. 2008). The large diamond shows the observed mass profile of Hydra A (current work) assuming hydrostatic equilibrium. Black and red open triangles correspond to cases in which the $f_{\text{gas}}(< r)$ value of Hydra A (current work) is the same as the cosmic mean baryon fraction (Komatsu et al. 2011) in the filament and the void directions, respectively.

Hydra A cluster and other clusters observed with weak-lensing (Okabe et al. 2010), and clusters observed with XMM by Ettori et al. (2011). An assumption of cluster dynamical state or hydrostatic equilibrium is not required in the weak-lensing results. The distribution of the $c - M$ relationship of these clusters agrees well with the relation expected from the numerical simulations by Duffy et al. (2008), although Ettori et al. (2011) found that relatively low-mass systems tend to have higher concentration parameters.

The hydrostatic mass in the Hydra A cluster of the filament and void directions are represented with the same NFW mass model with $c_{\text{vir}} = 9 - 10$ and $M_{\text{vir}} = (2.2 \pm 0.4) \times 10^{14} M_{\odot}$. As shown in Figure 14, this $c_{\text{vir}} - M_{\text{vir}}$ relationship of the Hydra A cluster was outside $\sigma(\log_{10} c) = 0.1$ within which most clusters from numerical simulations are distributed Duffy et al. (2008). If the hydrostatic mass was underestimated and the baryon fraction using the gravitational mass beyond r_{500} of the Hydra A cluster is the same as the cosmic mean baryon fraction in the two observed directions, the fits with the NFW model yielded smaller values of c_{vir} and higher values M_{vir} as shown in Figure 14. In this case, the derived value of M_{vir} in the filament direction became higher than that in the void direction. This result also indicates that the ICM in the outskirts of Hydra A deviates from hydrostatic equilibrium, and the X-ray emission and dark matter halo elongate in the same direction.

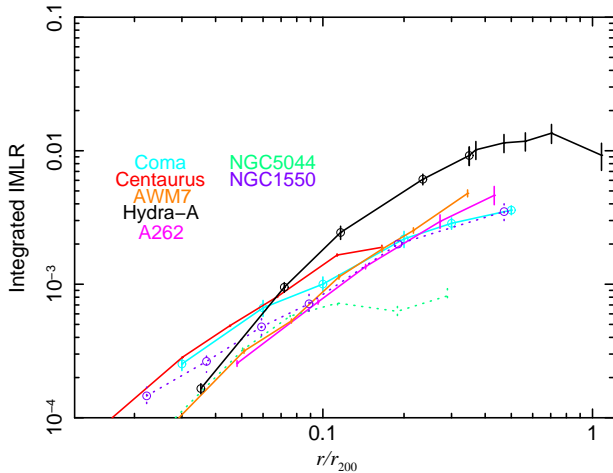


Fig. 15. Comparison of iron-mass-to-light-ratio for other clusters. The radius is scaled with the characteristic radius r_{200} (Henry et al. 2009). For comparison, we plotted the radial profile of cluster of galaxies AWM 7 (Sato et al. 2008, Sato et al. in preparation), Abell 262 (Sato et al. 2009b), the Centaurus cluster (Sakuma et al. 2011) and the Coma cluster (Matsushita et al. 2011) and galaxy groups NGC 5044 (Komiya et al. 2009) and NGC 1550 (Sato et al. 2010). Open circles are the result from XMM-Newton satellite, and others are Suzaku satellite.

5.5. Metal-Mass-to-Light Ratios out to the virial radius

We derived integrated IMLR, mass-to-light ratio for Fe, out to the virial radius for the first time. Here, we show the IMLR profile for the whole azimuthal angle to compare other clusters observed with Suzaku. Within $0.3 r_{200}$ and beyond $0.3 r_{200}$, we used the Fe abundances obtained by Matsushita (2011) and this work, respectively. Here, within $8'–15'$, or $0.35–0.65 r_{200}$, we used the weighted average of the Fe abundance at the three radial bins in this region. The error bars of the mass-to-light ratio include the errors in both the abundance and the K-band luminosity caused by the uncertainty in the contribution of fainter galaxies below the 2MASS threshold (see section 5.5 for details). Figure 15 shows the cumulative IMLR profile of the Hydra A cluster. The IMLR profile increases with radius within $0.4–0.5 r_{200}$, and becomes flatter beyond $0.5 r_{200}$ with the value of $\sim 0.01 M_{\odot}/L_{K,\odot}$, which reflects the flattening of the gas-mass-to-light ratio beyond r_{500} . For the void and filament directions, the IMLR profiles should increase with radius beyond r_{500} .

At r_{200} , the cumulative IMLR was $0.007–0.01 M_{\odot}/L_{K,\odot}$. A previously reported theoretical model predicts that the oxygen-mass-to-light ratio (OMLR) of a cluster is a sensitive function of the slope of the initial mass function (IMF) (Renzini 2005). Here, the oxygen mass is a sum of that trapped in stars and that in the ICM. By adopting a Salpeter IMF with a slope of 2.35, the expected value of the OMLR is $\sim 0.1 M_{\odot}/L_{B,\odot}$. In contrast, a top-heavy IMF with a slope of 1.35 overproduces metals more than that with a factor of 20. For the Hydra A cluster, by adopting the ratio of stellar-mass-to-light ratio 4–6 in the B-band and K-band (Nagino & Matsushita 2009; Matsushita et al. 2011), the IMLR in the B-band becomes $0.03–0.06 M_{\odot}/L_{B,\odot}$ and the cumulative OMLR within the virial radius becomes $\sim 0.1–0.3$

$(A_{\text{O}}/A_{\text{Fe}}) M_{\odot}/L_{B,\odot}$. Here, A_{O} and A_{Fe} are abundances of O and Fe in solar units, respectively. Beyond r_{500} of the Hydra A cluster, the integrated stellar mass is only several percent of the integrated gas mass. Thus, even by considering the difference of stellar metallicity and the abundance of the ICM, most of the metals in the cluster are in the ICM. Therefore, for cases with solar O/Fe ratio, the OMLR is similar to the expectations reported by Renzini (2005), assuming a Salpeter IMF in the Hydra A cluster. In contrast, by adopting the O/Fe ratio from a nucleosynthesis model of SN II with metallicity = 0.02, as reported by Nomoto et al. (2006), the OMLR within the virial radius becomes $0.3–1.0 M_{\odot}/L_{B,\odot}$ in the Hydra A cluster. This value is larger than the expectation from the Salpeter IMF, and is consistent with a flatter IMF slope.

In Figure 15, the cumulative IMLR profile of the Hydra A cluster was compared with those of other groups and clusters, including Coma (8 keV; Matsushita et al. 2011), Centaurus (4 keV; Sakuma et al. 2011), and AWM 7 clusters (3.6 keV; Sato et al. 2008), as well as NGC 1550 (1.2 keV; Sato et al. 2010) and NGC 5044 groups (1.0 keV; Komiya et al. 2009). Within $0.5 r_{200}$, the cumulative IMLR profile of the Hydra A cluster increased with radius by a factor of two higher than for other systems. No systematic dependence on the ICM temperature was evident for clusters with temperatures higher than 2 keV, although beyond $0.1 r_{200}$, a group of galaxies shows a significantly smaller IMLR.

The stellar and gas-mass fractions within r_{500} depend on the total system mass (Lin, Mohr, Stanford 2003; Lin & Mohr 2004; Vikhlinin et al. 2006; Sun et al. 2009; Giodini et al. 2009). These studies determined that within r_{500} the stellar-to-total-mass ratios of the groups are much larger than those in the clusters, whereas the gas-mass fraction increases with the system mass. The observed higher stellar mass fraction and the lower gas mass fraction within r_{500} in poor systems are occasionally interpreted as proof that the star formation efficiency depends on the system mass. However, as shown in Figure 11, the gas is more extended than the stars in a cluster within r_{500} . The gas density profiles in the central regions of groups and poor clusters were observed to be shallower than those in the self-similar model, and the relative entropy level was correspondingly higher than that in rich clusters (Ponman, Cannon, Navarro 1999; Ponman, Sanderson, Finoguenov 2003; Sun et al. 2009). Then, the difference in the ratio of gas-mass-to-stellar-mass may reflect differences in distributions of gas and stars, which in turn reflects the history of energy injection from galaxies to the ICM. To study the fractions of stars and gas in clusters of galaxies, and its dependence on the system mass, we need measurements of gas and stellar mass beyond r_{500} of other clusters.

6. Summary and Conclusion

We presented the results of the Suzaku observation of the Hydra A galaxy cluster, which is the first medium-sized cluster (temperature ~ 3 keV) observed with Suzaku out to the virial radius. Two observations were conducted, north-west and north-east offsets, which continue in a filament direction and a void direction of the large-scale structure of the Universe, respectively. We investigated possible azimuthal variations

in temperature, electron density, entropy and total mass profiles. Our analysis revealed that distributions of X-ray emission and galaxies elongate in the filament direction. The entropy profiles become flatter beyond r_{500} in contrast to the $r^{1.1}$ relationship expected from the shock heating model of the ICM. The entropy profiles are universal in clusters observed with Suzaku when scaled with the averaged temperature of each cluster. The hydrostatic masses in the two directions agree and the NFW universal matter profile represents the hydrostatic mass distribution obtained up to $1.8 r_{500}$, with $c_{\text{vir}} = 9 - 10$ and $M_{\text{vir}} = (2.2 \pm 0.4) \times 10^{14} M_{\odot}$. The gas fraction, $M_{\text{gas}}(< r)/M_{\text{H.E.}}(< r)$ significantly exceeds the cosmic mean baryon fraction of WMAP7 beyond $\sim r_{500}$. The flattening of the entropy profile and higher gas fraction contradict expectations based on numerical simulations. An underestimate of gas temperature due to the discrepancy between ion and electron temperatures gives higher entropy and smaller gas fraction at cluster outskirts. However, a flat or increasing temperature profile is required. If bulk motions caused by infalling matter from filaments of clusters are higher than that of numerical simulations, and if the ICM deviates from the hydrostatic equilibrium, the entropy becomes smaller and the gas fraction is overestimated. In addition, we obtained IMLR up to the virial radius for the first time, and compared our results with other clusters and groups. The IMLR profile is consistent within $0.5 r_{200}$ with other clusters, and become flatter from $0.5 r_{200}$ to r_{200} .

References

- Anders, E., & Grevesse, N., 1989, *Geochim. Cosmochim. Acta*, 53, 197
- Akahori, T., & Yoshikawa, K. 2010, *PASJ*, 62, 335
- Akamatsu, H., Hoshino, A., Ishisaki, Y., et al. 2011, *PASJ*, 63, 1019
- Balogh, M. L., Christlein, D., Zabludoff, A. I., & Zaritsky, D. 2001, *ApJ*, 557, 117
- Bautz, M. W., et al. 2009, *PASJ*, 61, 1117
- Borgani, S., Governato, F., Wadsley, J., et al. 2002, *MNRAS*, 336, 409
- Bullock, J. S., Kolatt, T. S., Sigad, Y., Somerville, R. S., Kravtsov, A. V., Klypin, A. A., Primack, J. R., & Dekel, A. 2001, *MNRAS*, 321, 559
- Burns, J. O., Skillman, S. W., & O'Shea, B. W., 2010, *ApJ*, 721, 1105
- David, L. P., et al. 2001, *ApJ*, 557, 546
- Dolag, K., Bartelmann, M., Perrotta, F., Baccigalupi, C., Moscardini, L., Meneghetti, & M., Tormen, G. 2004, *A&A*, 416, 853
- Duffy, A. R., Schaye, J., Kay, S. T., & Dalla Vecchia, C. 2008, *MNRAS*, 390, L64
- Eckert, D., Molendi, S., Gastaldello, F., & Rossetti, M. 2011, *A&A*, 529, A133
- Ettori, S., Gastaldello, F., Leccardi, A., et al. 2010, *A&A*, 524, A68
- Ettori, S., Gastaldello, F., Leccardi, A., Molendi, S., Rossetti, M., Buote, D., & Meneghetti, M. 2011, *A&A*, 526, 1
- Evrard, August E., Metzler, Christopher A. & Navarro, Julio F. 1996, *ApJ*, 469, 494
- Finoguenov, A., Arnaud, M. & David, L. P. 2001, *ApJ*, 555, 191
- Fukazawa, Y., Makishima, K., Tamura, T., Nakazawa, K., Ezawa, H., Ikebe, Y., Kikuchi, K. & Ohashi, T. 2000, *MNRAS*, 313, 21
- Fujita, Y., Tawa, N., Hayashida, K., et al. 2008, *PASJ*, 60, 343
- George, M. R., et al. 2009, *MNRAS*, 395, 657
- Giodini, S., et al. 2009, *ApJ*, 703, 982
- Gitti, M., Nulsen, P. E. J., David, L. P., McNamara, & B. R., Wise, M. W. 2011, *ApJ*, 732, 13
- Gonzalez, A. H., Zaritsky, D., & Zabludoff, A. I. 2007, *ApJ*, 666, 147
- Henry, J. P., Evrard, A. E., Hoekstra, H., Babul, A., & Mahdavi, A. 2009, *ApJ*, 691, 1307
- Hoshino, A., et al. 2010, *PASJ*, 62, 371
- Humphrey, P. J., Buote, D. A., Brighenti, F., et al. 2011, arXiv:1106.3322
- Ikebe, Y., Makishima, K., Ezawa, H., et al. 1997, *ApJ*, 481, 660
- Ishisaki, Y., et al. 2007, *PASJ*, 59, 113
- Kalberla, P. M. W., Burton, W. B., Hartmann, D., Arnal, E. M., Bajaja, E., Morras, R., & Pöppel, W. G. L. 2005, *A&A*, 440, 775
- Kawahara, H. 2010, *ApJ*, 719, 1926
- Kawaharada, M., et al. 2010, *ApJ*, 714, 423
- Kaiser, N. 1991, *ApJ*, 383, 104
- Katayama, H., Takahashi, I., Ikebe, Y., Matsushita, K., & Freyberg, M. J. 2004, *A&A*, 414, 767
- Kirkpatrick, C. C., Gitti, M., Cavagnolo, K. W., McNamara, B. R., David, L. P., Nulsen, P. E. J., & Wise, M. W. 2009, *ApJ*, 707, L69
- Komatsu, E., et al. 2011, *ApJ*, S192, 18
- Komiyama, M., Sato, K., Nagino, R., Ohashi, T. & Matsushita, K. 2009, *PASJ*, 61, 337
- Koyama, K., et al. 2007, *PASJ*, 59, 23
- Kushino, A., Ishisaki, Y., Morita, U., Yamasaki, N. Y., Ishida, M., Ohashi, T., & Ueda, Y. 2002, *PASJ*, 54, 327
- Lane, W. M., Clarke, T. E., Taylor, G. B., Perley, R. A., & Kassim, N. E. 2004, *AJ*, 127, 48
- Leccardi, A. & Molendi, S. 2008, *A&A*, 487, 461
- Lin, Y.-T., Mohr, J. J., & Stanford, S. A. 2003, *ApJ*, 591, 749
- Lin, L. T., & Mohr, J., J. 2004, *ApJ*, 617, 879
- Lodders, K. 2003, *ApJ*, 591, 1220
- Makishima, K. et al. 2001, *PASJ*, 53, 401
- Markevitch, M., Forman, W. R., Sarazin, C. L. & Vikhlinin, A. 1998, *ApJ*, 503, 77
- Matsushita, K. et al. 2007a, *PASJ*, 59, 327
- Matsushita, K. 2011, *A&A*, 527, A134
- Matsushita, K., Sato, T., Sakuma, E., & Sato, K., submitted to *PASJ*
- Maughan, B. J. et al. 2008, *MNRAS*, 387, 998
- McNamara, B. R. et al. 2000, *ApJ*, 534, L138
- Mitsuda, K., et al. 2007, *PASJ*, 59, 1
- Molnar, S. M., et al. 2009, *ApJ*, 696, 1640
- Myrium, G., et al. 2011, *ApJ*, 732, 13
- Nagai, D., & Lau, E. T. 2011, *ApJ*, 731, 10
- Nagai, D., Vikhlinin, A., & Krvtsov, A. V. 2007, *ApJ*, 655, 98
- Nagino, R., & Matsushita, K. 2009, *A&A*, 501, 157
- Nakamura, T. T., & Suto, Y. 1997, *Prog. Theor. Phys.* 97, 49
- Navarro, J. F., Frenk, C. S., & White, S. D. M. 1996, *ApJ*, 462, 563
- Navarro, J. F., Frenk, C. S., & White, S. D. M. 1997, *ApJ*, 490, 493
- Nomoto, K., Tominaga, N., Umeda, H., Kobayashi, C., & Maeda, K. 2006, *Nuclear Physics A*, 777, 424
- Nulsen, P. E. J., David, L. P., McNamara, B. R., Jones, C., Forman, W. R., & Wise, M. W. 2002, *ApJ*, 568, 163
- Nulsen, P. E. J., McNamara, B. R., Wise, M. W., & David, L. P. 2005, *ApJ*, 628, 629
- Okabe, N., et al. 2010, *PASJ*, 60, 1133
- Peres, C. B., Fabian, A. C., Edge, A. C., Allen, S. W., Johnstone, R. M., & White, D. A. 1998, *MNRAS*, 298, 416
- Pratt, G. W., Böhringer, H., Croston, J. H., Arnaud, M., Borgani, S., Finoguenov, A., & Temple, R. F. 2007, *A&A*, 461, 71
- Pointecouteau, E., Arnaud, M., & Pratt, G. W. 2005, *A&A*, 435, 1
- Ponman, T. J., Cannon, D. B., & Navarro, J. F. 1999, *Nature*, 397, 135
- Ponman, T. J., Sanderson, A. J. R., & Finoguenov, A. 2003, *MNRAS*, 343, 331
- Reiprich, T. H., et al. 2009, *A&A*, 501, 899

- Renzini, A. 2005, *The Initial Mass Function 50 Years Later*, Edited by E. Corbelli and F. Palle, INAF Osservatorio Astrofisico di Arcetri, Firenze, Italy; H. Zinnecker, Astrophysikalisches Potsdam, Germany. *Astrophysics and Space Science Library* Volume 327. Published by Springer, Dordrecht, 2005, p.221
- Ryu, D., et al. 2003, *ApJ*, 593, 599
- Sakuma, E., Ota, N., Sato, K., Sato, T., & Matsushita, K. 2011, *PASJ*, 63, 979
- Sato, K. et al. 2007, *PASJ*, 59, 299
- Sato, K., Matsushita, K., Ishisaki, Y., Yamasaki, N. Y., Ishida, M., Sasaki, S. & Ohashi, T. 2008, *PASJ*, 60, 333
- Sato, K., Matsushita, K., Ishisaki, Y., Yamasaki, N. Y., Ishida, M. & Ohashi, T. 2009a, *PASJ*, 61, 353
- Sato, K., Matsushita, K. & Gastaldello, F. 2009b, *PASJ*, 61, 365
- Sato, K., Kawaharada, M., Nakazawa, K., Matsushita, K., Ishisaki, Y., Yamasaki, N. Y. & Ohashi, T. 2010, *PASJ*, 62, 1445
- Sato, T., Matsushita, K., Ota, N., Sato, K., Nakazawa, K. & Sarazin, C. L. 2011, *PASJ*, 63, 991
- Sato K., Matsushita, K., Yamasaki, N. Y., Sasaki, S., & Ohashi, T., submitted to *PASJ*
- Schelegel, D. J., Finkbeiner, D. P., & Davis, M. 1998, *ApJ*, 500, 525
- Simionescu, A., Werner, N., Böhringer, H., Kaastra, J. S., Finoguenov, A., Brüggén, M. & Nulsen, P. E. J. 2009, *A&A*, 493, 409
- Simionescu, A., Roediger, E., Nulsen, P. E. J., Brüggén, M., Forman, W. R., Böhringer, H., Werner, N., & Finoguenov, A. 2009, *A&A*, 495, 721
- Simionescu, A., et al. 2011, *Science*, 331, 1576
- Smith, R. K., Brickhouse, N. S., Liedahl, D. A., & Raymond, J. C. 2001, *ApJL*, 556, L91
- Sun, M., Voit, G. M., Donahue, M., Jones, C., Forman, W., & Vikhlinin, A. 2009, *ApJ*, 693, 1142
- Takizawa, M., & Mineshige, S. 1998, *ApJ*, 499, 82
- Takizawa, M. 1998, *ApJ*, 509, 579
- Takizawa, M. 1999, *ApJ*, 520, 514
- Tamura, T., et al. 2008, *PASJ*, 60, 317
- Tawa, N. 2008, PhD Thesis, University of Osaka
- Tawa, N., et al. 2008, *PASJ*, 60, S11
- Taylor, G. B., Perley, R. A., Inoue, M., Kato, T., Tabara, H., & Aizu, K. 1990, *ApJ*, 360, 41
- Tozzi, P., & Norman, C. 2001, *ApJ*, 546, 63
- Trentham, N., & Mobasher, B. 1998, *MNRAS*, 299, 488
- Urban, O., Werner, N., Simionescu, A., Allen, S. W., & Böhringer, H. 2011, *MNRAS*, 414, 2101
- Vazza, F., Brunetti, G., Kritsuk, A., Wagner, R., Gheller, C., & Norman, M. 2009, *A&A*, 504, 33
- Vikhlinin, A., Markevitch, M., Murray, S. S., Jones, C., Forman, W. & Van Speybroeck, L. 2005, *ApJ*, 628, 655
- Vikhlinin, A., Kravtsov, A., Forman, W., Jones, C., Markevitch, M., Murray, S. S., & Van Speybroeck, L. 2006, *ApJ*, 640, 691
- Voit, G. M., Kay, S. T., & Bryan, G. L. 2005, *MNRAS*, 364, 909
- Wise, M. W., McNamara, B. R., Nulsen, P. E. J., Houck, J. C., & David, L. P. 2007, *ApJ*, 659, 1153
- Yoshino, T., et al. 2009, *PASJ*, 61, 805
- Zhang, Y.-Y., Okabe, N., Finoguenov, A., et al. 2010, *ApJ*, 711, 1033

Suzaku observations of the Hydra A cluster out to the virial radius

Takuya SATO¹, Toru SASAKI¹, Kyoko MATSUSHITA¹, Eri SAKUMA¹, Kosuke SATO¹,
Yutaka FUJITA², Nobuhiro OKABE³, Yasushi FUKAZAWA⁴, Kazuya ICHIKAWA¹,
Madoka KAWAHARADA⁵, Kazuhiro NAKAZAWA⁶, Takaya OHASHI⁷, Naomi OTA⁸,
Motokazu TAKIZAWA⁹, and Takayuki TAMURA⁵

¹*Department of physics, Tokyo University of Science, 1-3 Kagurazaka, Shinjuku-ku, Tokyo 162-8601, Japan*
j1209703@ed.kagu.tus.ac.jp; matusita@rs.kagu.tus.ac.jp

²*Department of Earth and Space Science, Graduate School of Science, Osaka University, Toyonaka, Osaka 560-0043, Japan*

³*Institute of Astronomy and Astrophysics, Academia Sinica, P.O. Box 23-141, Taipei 106, Taiwan; Astronomical Institute, Tohoku University, Aramaki, Aoba-ku, Sendai, 980-8578, Japan*

⁴*Department of Physical Science, Hiroshima University, 1-3-1 Kagamiyama, Higashi-Hiroshima, Hiroshima 739-8526, Japan*

⁵*Institute of Space and Astronautical Science, Japan Aerospace Exploration Agency, 3-1-1 Yoshinodai, Chuo-ku, Sagami-hara, Kanagawa 252-5210, Japan*

⁶*Department of Physics, The University of Tokyo, 7-3-1 Hongo, Bunkyo-ku, Tokyo 113-0033, Japan*

⁷*Department of Physics, Tokyo Metropolitan University, 1-1 Minami-Osawa, Hachioji, Tokyo 192-0397, Japan*

⁸*Department of Physics, Nara Women's University, Kitauoyanishi-machi, Nara, Nara 630-8506, Japan*

⁹*Department of Physics, Yamagata University, Yamagata, Yamagata 990-8560, Japan*

(Received —; accepted —)

Abstract

We report Suzaku observations of the northern half of the Hydra A cluster out to ~ 1.4 Mpc, reaching the virial radius. This is the first Suzaku observations of a medium-size ($kT \sim 3$ keV) cluster out to the virial radius. Two observations were conducted, north-west and north-east offsets, which continue in a filament direction and a void direction of the large-scale structure of the Universe, respectively. The X-ray emission and distribution of galaxies elongate in the filament direction. The temperature profiles in the two directions are mostly consistent with each other within the error bars and drop to 1.5 keV at $1.5 r_{500}$. As observed by Suzaku in hot clusters, the entropy profile becomes flatter beyond r_{500} , in disagreement with the $r^{1.1}$ relationship that is expected from accretion shock heating models. When scaled with the average intracluster medium (ICM) temperature, the entropy profiles of clusters observed with Suzaku are universal and do not depend on system mass. The hydrostatic mass values in the void and filament directions are in good agreement, and the Navarro, Frenk, and White universal mass profile represents the hydrostatic mass distribution up to $\sim 2 r_{500}$. Beyond r_{500} , the ratio of gas mass to hydrostatic mass exceeds the result of the Wilkinson microwave anisotropy probe, and at r_{100} , these ratios in the filament and void directions reach 0.4 and 0.3, respectively. We discuss possible deviations from hydrostatic equilibrium at cluster outskirts. We derived radial profiles of the gas-mass-to-light ratio and iron-mass-to-light ratio out to the virial radius. Within r_{500} , the iron-mass-to-light ratio of the Hydra A cluster was compared with those in other clusters observed with Suzaku.

Key words: galaxies: clusters: individual (Hydra A cluster) — X-rays: galaxies: clusters — intergalactic medium

1. Introduction

Clusters of galaxies are the largest self-gravitating systems in the Universe, and offer unique information on the process of structure formation governed by cold dark matter (CDM). In addition, these clusters are considered as a laboratory for studying thermal and chemical evolutions of the Universe in which baryons play the most important role. X-ray observations provide valuable information about the structure formation, gas heating and cooling, and metal enrichment of galaxy clusters. Because the dynamical time-scale of clusters is comparable to the Hubble time, cluster outskirts should maintain original records of cluster evolution via accretion of gas and substructures from filaments of the surrounding large-scale structure of the Universe.

Thanks to the low and stable background of the X-ray

Imaging Spectrometer (XIS; Koyama et al. 2007), Suzaku (Mitsuda et al. 2007) was able to unveil for the first time the intracluster medium (ICM) beyond r_{500} , a radius within which the mean cluster-mass density is 500 times the cosmic critical density. The accurate calibration of the XIS also allows precise measurements of the ICM temperature (Sato et al. 2011). Suzaku derived the temperature and entropy profiles of the ICM of several massive clusters up to the virial radius (George et al. 2009; Reiprich et al. 2009; Bautz et al. 2009; Kawaharada et al. 2010; Hoshino et al. 2010; Simionescu et al. 2011; Akamatsu et al. 2011). From the center to r_{200} , a systematic drop in temperature was found by a factor of ~ 3 , and the observed entropy profiles become flatter beyond r_{500} . These profiles are lower than the entropy profile predicted by the numerical simulations of gravitational collapse (Tozzi & Norman 2001; Voit, Kay, Bryan 2005), which is pro-

portional to $r^{1.1}$. Kawaharada et al. (2010) discovered that beyond r_{500} of the Abell 1689 cluster, the total mass obtained from weak-lensing observations with Subaru is larger than that calculated assuming hydrostatic equilibrium. Therefore, one explanation for the low entropy profiles at cluster outskirts is that infalling matter retained some of its kinetic energy in bulk motion (Bautz et al. 2009; George et al. 2009; Kawaharada et al. 2010). Based on Suzaku observations of the Perseus cluster, Simionescu et al. (2011) proposed a gas-clumping effect as an additional interpretation. Hoshino et al. (2010) and Akamatsu et al. (2011) discussed possible deviations of electron temperature from ion temperature to explain the observed lower temperature and entropy profiles. To clarify these effects in the outskirts, dependence on the system mass or on the ICM temperature should be examined. With XMM-Newton observations, Urban et al. (2011) found a similar flattening of the entropy profile in one direction in the Virgo cluster ($kT = 2.3$ keV). However, Humphrey et al. (2011) detected no evidence of flat profiles at large scales ($> r_{500}$) in the relaxed fossil group or in the poor cluster, RXJ 1159+5531. Therefore, more samples of medium-sized clusters are required.

In addition to measuring the temperature and entropy profiles, Suzaku measured the abundance of Fe in the ICM beyond $0.5r_{180}$ (Fujita et al. 2008; Tawa et al. 2008; Simionescu et al. 2011). Metal abundances in the ICM also provide important information on the chemical history and evolution of clusters. The ASCA satellite first measured the distribution of Fe in the ICM (Fukazawa et al. 2000; Finoguenov et al. 2001). Recently, spatial distributions of Fe from 0.3 to $0.4 r_{180}$ have been studied with the XMM-Newton and Chandra satellites (Vikhlinin et al. 2005; Maughan et al. 2008; Leccardi & Molendi 2008; Matsushita 2011). Since metals are synthesized by supernovae (SNe) in galaxies, the ratios of metal mass in the ICM to the total light from galaxies in clusters or groups, (i.e., metal-mass-to-light ratios) are key parameters in investigating the chemical evolution of the ICM. Suzaku measured the iron-mass-to-light ratios (IMLR) of several clusters and galaxy groups out to $0.2 \sim 0.5 r_{180}$ (Matsushita 2007; Komiyama et al. 2009; Sato et al. 2007; Sato et al. 2008; Sato et al. 2009a; Sato et al. 2009b; Sato et al. 2010; Sakuma et al. 2011), and with XMM-Newton, the IMLR of the Coma cluster out to $0.5r_{180}$ was derived (Matsushita et al. 2011). The IMLR profiles increase with radius, indicating that Fe in the ICM extends farther than stars.

The Hydra A cluster ($z = 0.0539$) with an ICM temperature of ~ 3 keV is one of the prototype cool-core clusters in which McNamara et al (2000) discovered a displacement of X-ray gas in the central region through the radio lobes from the central active galactic nucleus (AGN). This cluster is also known as Abell 780 and remains a major examples of AGN interaction that is studied through radio and X-rays (Taylor et al. 1990; David et al. 2001; Nulsen et al. 2002; Nulsen et al. 2005; Lane et al. 2004; Wise et al. 2007; Simionescu et al. 2009a; Simionescu et al. 2009b; Kirkpatrick et al. 2009). Through Chandra and XMM-Newton observations, a sharp X-ray surface-brightness edge was detected at radii between $4.3'$ and $6'$ (200–300 kpc) and was interpreted as a shock wave caused by an AGN outburst. The abundances of the Hydra A cluster was measured within $\sim 0.3 r_{180}$ with XMM (Simionescu et al. 2009b; Matsushita 2011).

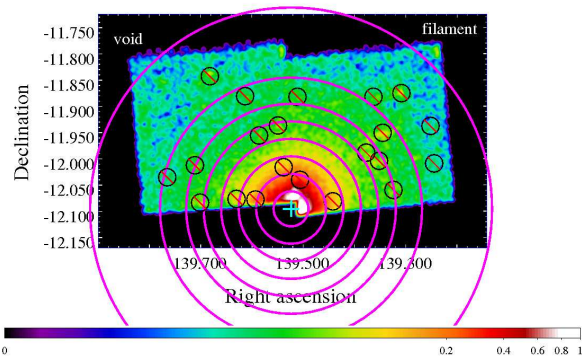


Fig. 1. XIS0 image of the Hydra A cluster within 0.5–4.0 keV energy range. The light blue cross indicates the X-ray peak of the cluster. Differences in the vignetting effect are uncorrected. Regions of spectral accumulation are shown as magenta rings. The ring radii are $2'$, $4'$, $6'$, $8'$, $10'$, $12'$, $15'$ and $23'$. Black circles represent excluded regions around point sources.

This paper reports the results of two Suzaku observations in the northern half of the Hydra A cluster out to $25'$ (≈ 1.5 Mpc), which corresponds to the virial radius. The observations were conducted using the XIS. This study reports the first Suzaku observations of a medium-sized cluster with an average temperature of ~ 3 keV up to the virial radius. The two observed fields continue in a filament direction that continues to the Abell 754 cluster and a void direction of the large-scale structure of the Universe (see Figure 9).

In this study, we use the Hubble constant, $H_0 = 70 \text{ km s}^{-1} \text{ Mpc}^{-1}$, $\Omega_m = 0.27$ and $\Omega_\Lambda = 0.73$. The luminosity distance D_L and angular size distance D_A to the Hydra A cluster are $D_L = 240$ Mpc and $D_A = 217$ Mpc, respectively, and $1'$ corresponds to 66.6 kpc. We use the epoch J2000.0 for the right ascension and declination of the equatorial coordinate system. In addition, we use the solar abundance table by Lodders (2003), in which the solar Fe abundance relative to H is 2.95×10^{-5} . Considering a difference in solar He abundance, the Fe abundance yielded by Lodders (2003) is 1.5 times higher than that using the photo-spheric value by Anders & Grevesse (1989). Errors were quoted at a 90% confidence level for a single parameter.

2. Observation and Data Reduction

2.1. Suzaku observations

Suzaku conducted two observations of the Hydra A cluster in November 2010, which was during the Suzaku Phase-V period. The details of the observations are summarized in Table 1. The first observation, HYDRA A-1, was $12'$ north-west offset from the X-ray peak of the Hydra A cluster with coordinates (RA, Dec) = (139.5236, -12.0955) in degrees. The second observation, HYDRA A-2, was $12'$ north-east offset from the X-ray peak of the Hydra A cluster. The north-west and north-east fields continue into the filament and void structures, respectively (See figure 9). Hereafter, we refer to the north-west and north-east offsets as filament and void, respectively.

Table 1. Observation log of the Hydra A cluster

Field name	Target name	Sequence number	Observation date	RA* (deg)	Dec* (deg)	Exposure (ks)
North-west (filament)	HYDRA A-1	805007010	2010-11-08	139.3723	-11.9472	35.6
North-east (void)	HYDRA A-2	805008010	2010-11-09	139.6749	-11.9472	34.9

* Coordinates are referred to J2000.0.

The XIS, which was operated in its normal mode during the observations, consists of three sets of X-ray CCD (XIS0, XIS1, and XIS3). XIS1 is a back-illuminated (BI) sensor, while both XIS0 and XIS3 are front-illuminated (FI) sensors. Data reduction was done with HEASoft version 6.11. The XIS event lists created by rev 2.5 pipeline processing were filtered using the following additional criteria: a geomagnetic cutoff rigidity (COR2) > 6 GV, and an elevation angle $> 10^\circ$ from the earth limb. The 5×5 and 3×3 editing modes data formats were added. The exposure times after data selection are shown in Table 1.

To obtain the temperature and electron density profiles, we accumulated spectra within annular regions centered on the X-ray peak as shown in Figure 1. Regions around calibration sources and the innermost region within $2'$ were excluded from the spectral analysis. The reason for this exclusion is that we could not obtain sufficient photon statistics to analyze the spectra (which have multiphase features at the cluster center) because the given area was detected on the edge of a CCD chip in our observation. In addition, Suzaku's PSF is also insufficient to resolve such a complex structure. However, with their powerful imaging capability, Chandra and XMM observations have unveiled such complex features in the central region. Using the ewavelet tool in SAS¹, we searched for point-like sources in the Suzaku images in the energy range of 2.0–10.0 keV. In this energy range, the flux levels were approximately $> 2 \times 10^{-14}$ erg cm⁻² s⁻¹. These point sources were excluded as circular regions with radii of $1'$ (figure 1). The non X-ray background (NXB) was subtracted from each spectrum using a database of night Earth observations with the same detector area and COR distribution (Tawa et al. 2008).

We included the degradation of energy resolution due to radiation damage in the redistribution matrix file (RMF) generated by the `xisrmfgen` Ftools task. In addition, we created an ancillary response file (ARF) using the `xissimarfgen` Ftools task (Ishisaki et al. 2007). A decrease in the low-energy transmission of the XIS optical blocking filter (OBF) was also included in the ARF. For filament and void fields, we generated ARF files assuming uniformly extended emission from an enriched region with a $20'$ radius. We used the XSPEC_v12.7.0 package and ATOMDB_v2.0.1 for spectral analysis. Each spectrum was binned and each spectral bin contained a minimum of 50 counts. To avoid systematic uncertainties in the background, we ignored energy ranges above 7 keV and below 0.7 keV. In addition, we excluded the narrow energy band between 1.82 and 1.84 keV in the fits because of the incomplete response around the Si edge.

¹ <http://xmm.esa.int/sas/>

2.2. XMM observations

We used the same data and analysis as that reported by Matsushita (2011). The XMM-Newton archival data of Hydra A (observation identifier 0109980301) had exposure times of 14.0 ks, 19.1 ks and 22.2 ks for MOS1, MOS2 and PN, respectively, after background flares were screened out. We selected events with patterns smaller than 5 and 13 for the PN and MOS, respectively. Spectra were accumulated in concentric annular regions of $0'-0.5'$, $0.5'-1'$, $1'-1.5'$, $1.5'-2'$, $2'-3'$, $3'-4'$, $4'-5'$, $5'-6'$, $6'-7'$, $7'-8'$, and $8'-9'$, centered on the X-ray peak of the Hydra A cluster. Here, the X-ray peaks were derived using the ewavelet tool of SAS-v8.0.0, and luminous point sources were excluded. The spectra from MOS1 and MOS2 were added. The background spectrum for each annular region was calculated by integrating blank-sky data in the same detector region. From deep-sky observations with XMM-Newton, we selected the data having background most similar to that of the Hydra A cluster and the faintest Galactic emission, after screening out background flare events from the data and the background, following Katayama et al. (2004). Next, we scaled the background using a count rate between 10 and 12 keV.

The response matrix file and the ARF corresponding to each spectrum were calculated using SAS-v8.0.0. Further details appear in sections 2 and 3 of Matsushita (2011).

3. Data Analysis

3.1. Estimation of background spectra

To derive the radial profiles of the temperature, electron density, and Fe abundance of the ICM, we fitted the NXB-subtracted spectra with a thermal plasma model (APEC; Smith et al. 2001).

We first fitted the spectra in the outermost ring ($15'-23'$ region) to determine the local X-ray background. As reported by Yoshino et al. (2009), the background emission of Suzaku XIS can be fitted with a three-component model: two thermal plasma models (APEC; Smith et al. 2001) for the local hot bubble (LHB) and the solar wind charge exchange (SWCX), the Milky Way Halo (MWH), and a power-law model for the extragalactic cosmic X-ray background (CXB). MWH and CXB components were convolved with an photoelectric absorption in the Galaxy, N_H . Therefore, we adopted the model formula, $apec_{LHB} + wabs \times (apec_{MWH} + power-law_{CXB})$ as background. We assumed a zero redshift and a solar abundance for LHB and MWH components. The temperature of the LHB and MWH was fixed at 0.1 keV and 0.3 keV, respectively. The column density of the Galactic neutral hydrogen was fixed at 4.7×10^{20} cm⁻² (Kalberla et al. 2005), and the photon index of the CXB component was fixed at 1.41 (Kushino et al. 2002). Using the formula $apec_{LHB} + wabs \times (apec_{ICM} + apec_{MWH} +$

Table 2. Resultant parameters of the background components.

Cosmic X-ray Background	Local Hot Bubble	Milky-Way halo	
normalization*	normalization [†]	normalization [†]	Reduced- χ^2
	$\times 10^{-3}$	$\times 10^{-4}$	$\chi^2/\text{d.o.f}$
$8.92^{+0.72}_{-0.85}$	$8.93^{+6.02}_{-5.75}$	$1.83^{+1.85}_{-1.72}$	1.04(144/139)

* Measured at 1keV with unit of photons $\text{cm}^{-2} \text{s}^{-1} \text{keV}^{-1} \text{sr}^{-1}$.

[†] Normalization of the APEC component divided by the solid angle, Ω^U , assumed in the uniform-sky ARF calculation (20' radius), $Norm = \int n_e n_H dV / (4\pi(1+z)^2 D_A^2) / \Omega^U \times 10^{-14} \text{ cm}^{-5} 400\pi \text{ arcmin}^{-2}$, where D_A is the angular distance to the source.

power-law_{CXB}), we fitted the spectra with a sum of the background components and a single-temperature APEC model for the ICM. Temperature and normalization of the ICM component were allowed to vary, and redshift was fixed at 0.0539. Normalizations of the background components were also left free. The spectra of the filament and void fields were fitted simultaneously, and each parameter of background and abundance of the ICM was assumed to be the same.

Results of the spectral fit are shown in Figure 2. The resulting parameters for the background and ICM are shown in Table 2 and 3, respectively. The normalizations obtained for the CXB and the Galactic components are consistent with those derived by Kushino et al. (2002) and Yoshino et al. (2009), respectively.

Several blank fields observed with Suzaku contained emission with $kT = 0.6 - 0.8 \text{ keV}$ (Yoshino et al. 2009). Therefore, we added an APEC component with $kT = 0.6 \text{ keV}$ and refitted the outermost spectra. The normalization of the 0.6 keV component had a much smaller value than the other Galactic components, and the temperatures and normalizations of the ICM did not change.

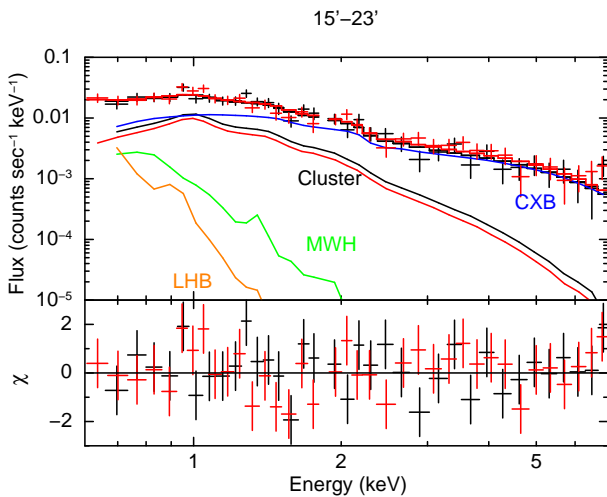


Fig. 2. NXB-subtracted spectra of XIS1 (crosses) for the outermost ring (15'–23' region), fitted by the $apec_{LHB} + wabs \times (apec_{ICM} + apec_{MWH} + power-law_{CXB})$ model (stepped solid lines). Black and red colors correspond to the directions in the filament and void, respectively. The bottom panel shows residuals of the fit. The contributions of the ICM are plotted as black and red solid lines, those of the Galactic emission as orange and green lines, and those of the CXB as blue lines.

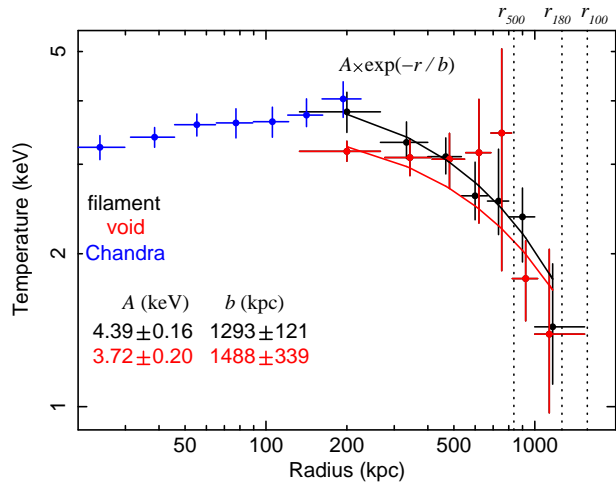


Fig. 4. Radial temperature profiles of the filament (black) and void (red) directions. Solid lines show the best fit function of $A \times \exp(-b \times r)$. Chandra results (David et al. 2001) are plotted in blue. Vertical dotted lines show r_{500} , r_{180} , and r_{100} , derived from the fitting of the hydrostatic mass with the NFW universal mass profile (Navarro et al. 1997), as described in subsection 4.4.

3.2. Spectral fits of annular regions

We fitted the XIS spectra in each region of the Hydra A cluster using a single-temperature APEC model for the ICM with the Galactic absorption, N_H . The spectra of each annular region of the two fields were fitted simultaneously by minimizing the total χ^2 value. Here, the common background model was included for all regions, where the surface brightness of the background components were restricted within the statistical errors derived for the outermost regions. The temperature and normalization of the ICM component were free parameters. The abundances in each annular region in the two fields were assumed to have the same value. N_H was fixed to the Galactic value of $4.7 \times 10^{20} \text{ cm}^{-2}$ in the direction of the Hydra A cluster.

The resultant parameters are summarized in Table 3, and the best-fit spectra are shown in Figure 3. The spectra are well represented with the single-temperature model for the ICM and the background.

4. Results

4.1. Temperature profile

Figure 4 shows the radial temperature profiles of the two directions derived from the spectral fits. At a given radius, the temperatures for each direction are consistent within statisti-

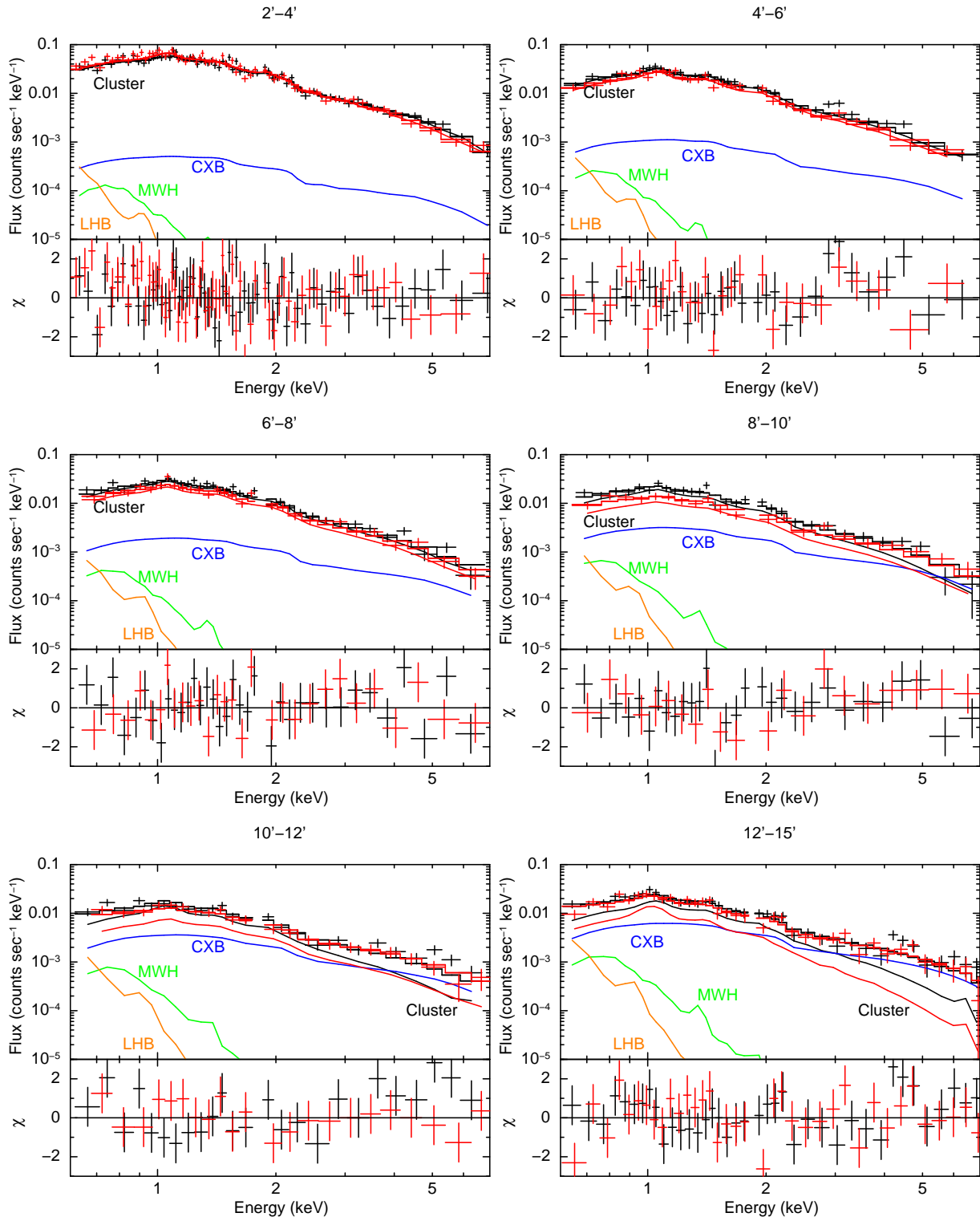


Fig. 3. NXB-subtracted XIS1 spectra fitted with the single temperature (APEC) model for the ICM. Black and red colors correspond to directions toward the filament and void, respectively. Lower panels in each diagram show residual of fit. The contributions of the ICM are plotted as red and black solid lines, while those of the galactic emission and the CXB are plotted as orange, green and blue lines, respectively.

Table 3. Parameters resulting from fitting ICM with the single-temperature APEC model in the energy ranges of 0.7–7.0 keV.

Region		filament			void		
(arcmin)	(kpc)	kT (keV)	abundance (solar)	normalization*	kT (keV)	normalization*	$\chi^2/\text{d.o.f.}$
2' – 4'	133 – 266	$3.81^{+0.35}_{-0.34}$	0.33 ± 0.10	$0.45^{+0.02}_{-0.02}$	$3.18^{+0.15}_{-0.14}$	$0.36^{+0.02}_{-0.02}$	1.22(263/216)
4' – 6'	266 – 400	$3.31^{+0.32}_{-0.23}$	0.43 ± 0.43	$0.10^{+0.01}_{-0.01}$	$3.09^{+0.27}_{-0.24}$	$0.090^{+0.01}_{-0.01}$	1.09(146/134)
6' – 8'	400 – 533	$3.11^{+0.28}_{-0.23}$	0.28 ± 0.15	$0.056^{+0.004}_{-0.005}$	$3.07^{+0.38}_{-0.31}$	$0.035^{+0.003}_{-0.003}$	1.18(177/150)
8' – 10'	533 – 666	$2.60^{+0.43}_{-0.27}$	0.18 ± 0.13	$0.025^{+0.003}_{-0.003}$	$3.16^{+0.86}_{-0.81}$	$0.015^{+0.003}_{-0.002}$	1.18(129/109)
10' – 12'	666 – 799	$2.54^{+0.67}_{-0.36}$	0.38 ± 0.38	$0.013^{+0.003}_{-0.002}$	$3.46^{+1.60}_{-1.60}$	$0.0058^{+0.0016}_{-0.0012}$	1.07(99/93)
12' – 15'	799 – 997	$2.36^{+0.33}_{-0.44}$	0.30 ± 0.19	$0.010^{+0.001}_{-0.001}$	$1.79^{+0.33}_{-0.31}$	$0.0048^{+0.0012}_{-0.0012}$	1.13(170/150)
15' – 23'	997 – 1529	$1.44^{+0.47}_{-0.33}$	0.10 ± 0.08	$0.0036^{+0.0012}_{-0.0011}$	$1.39^{+0.65}_{-0.42}$	$0.0025^{+0.0011}_{-0.0008}$	1.19(263/221)

* Normalization of the APEC, component divided by the solid angle, Ω^U , assumed in the uniform-sky ARF calculation ($20'$ radius), $Norm = \int n_e n_H dV / (4\pi(1+z)^2 D_A^2) / \Omega^U \times 10^{-14} \text{ cm}^{-5} 400\pi \text{ arcmin}^{-2}$, where D_A is the angular distance to the source.

cal errors, except around ~ 200 kpc from the center. The region around 200 kpc corresponds to the shock front detected by Chandra and XMM in the filament direction (Simionescu et al. 2009b; Gitti et al. 2011). From 300 kpc to 1200 kpc, the temperatures in each direction decrease with radius in a similar manner down to ~ 1.4 keV.

From ROSAT observations, Ikebe et al. (1997) found that the spectrum at the central region within $2'$ exhibits the multiphase feature. Although the central $2'$ region was excluded in our spectral analysis, we examined the spectral fits with the two-temperature model in regions with $r > 2'$. The reduced- χ^2 for the two-temperature model was not significantly improved in comparison with the single-temperature model.

To determine the hydrostatic mass of Hydra A, we fitted the temperature profile of each direction with the exponential formula, $A \times \exp(-b \times r)$, where A and b are free parameters with units of keV and kpc^{-1} , respectively, and r is the distance from the X-ray peak of the cluster center. The resulting fit parameters and best-fit functions are shown in Figure 4. In the filament direction, the normalization factor A of the exponential model was 18% higher than that in the void direction, which reflects a temperature difference of ~ 200 kpc. The parameter b for both directions is consistent within statistical error.

4.2. Deprojected electron density profile

We calculated three-dimensional electron density profiles from the normalization of the ICM component derived with Suzaku, considering the geometrical volume that contributes to each two-dimensional region. Here, we assumed spherical symmetry within each field. The electron density profile was also obtained using XMM data. To avoid uncertainties in the background, we fitted the annular spectra of XMM MOS with the APEC model in an energy range of 1.6–5.0 keV. Here, the temperature and Fe abundance were left free within the error bars derived by Matsushita (2011). We fitted the derived emissivity profiles with a double- β -model, and calculated the three-dimensional radial profile of the electron-density.

Figure 5 shows the electron density profile derived from XMM and Suzaku (this work), Chandra (David et al. 2001) and the ROSAT surface-brightness profile scaled with the XMM density profile at 200 kpc (Ikebe et al. 1997). The deprojected electron density profile derived from XMM and Suzaku observations agree well with those from ROSAT within 500 kpc and from Chandra within 200 kpc.

At a given distance from the X-ray peak, electron density

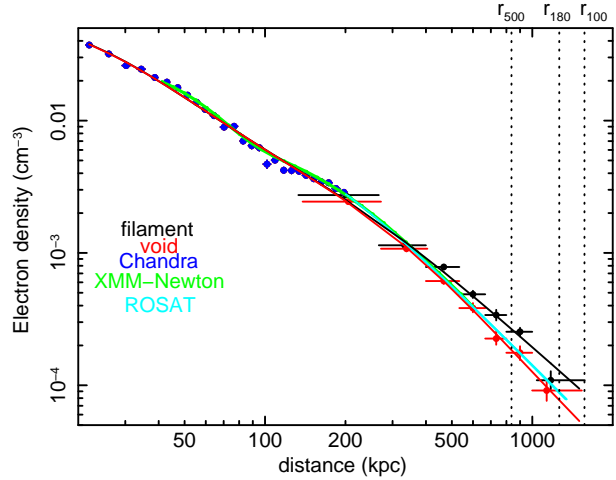


Fig. 5. Deprojected electron density profile of the filament (black) and void (red) directions. Black and red solid lines show the best fit with the double- β model. Green solid line shows the electron density profile derived with XMM data, the light blue solid line shows that derived from the ROSAT surface-brightness profile (Ikebe et al. 1997) scaled with the XMM profile, and the blue filled circles show that derived from Chandra results (David et al. 2001).

beyond 400 kpc in the filament direction was systematically higher than that in the void direction, reflecting the difference in normalizations (Table 3 and Figure 3). At 900 kpc, for example, the deprojected electron densities in the filament and void directions were $(2.54 \pm 0.18) \times 10^{-4} \text{ cm}^{-3}$ and $(1.76 \pm 0.21) \times 10^{-4} \text{ cm}^{-3}$, respectively. The electron density dropped to $\sim 10^{-4} \text{ cm}^{-3}$ around 1200 kpc.

We fitted the density profiles from XMM and Suzaku results with the double- β model from 40 to 1200 kpc. The results are shown in Figure 5, and the resulting parameters are given in Table 4. From 400 kpc to 1530 kpc, the radial profiles of the electron density are also well represented by a power-law profile with slopes of $\Gamma = 1.60 \pm 0.05$ and 1.72 ± 0.07 in the filament and void directions, respectively. The slope of the electron density in the void direction was slightly steeper than that in the filament direction. Fitting the electron density profiles beyond 100 kpc with the single β -model resulted in $\beta = 0.61 \pm 0.02$ and $\beta = 0.74 \pm 0.03$ for the filament and void directions, respectively. These values are close to the value of 0.68 derived from the ROSAT surface-brightness profile (Ikebe et al. 1997).

Table 4. Parameters resulting from fitting the deprojected density profile derived from XMM and Suzaku with the double- β model*.

Field	narrower component			wider component		
	$n_{0,1}$ (10^{-2} cm $^{-3}$)	$r_{c,1}$ (kpc)	β_1	$n_{0,2}$ (10^{-3} cm $^{-3}$)	$r_{c,2}$ (kpc)	β_2
void	6.73 ± 0.17	21.3 ± 4.7	0.59 ± 0.01	2.16 ± 0.14	278 ± 264	0.95 ± 0.07
filament	6.61 ± 0.19	22.3 ± 5.4	0.62 ± 0.01	2.73 ± 0.15	193 ± 114	0.60 ± 0.03

* double- β model is given by the form $n(r) = n_{0,1}(1 + (r/r_{c,1})^2)^{-3\beta_1/2} + n_{0,2}(1 + (r/r_{c,2})^2)^{-3\beta_2/2}$.
The errors of $n_{0,1}$ and β_1 are calculated by fixing the $r_{c,1}$ and wider component, and vice versa.

Table 5. Resultant fit parameters of the deprojected density profile derived from XMM and Suzaku with the single- β model* beyond 100 kpc.

Field	n_0 (10^{-3} cm $^{-3}$)	r_c (kpc)	β
void	7.38 ± 0.42	160 ± 13	0.74 ± 0.03
filament	7.98 ± 0.50	131 ± 10	0.61 ± 0.02

* single- β model is given by the form $n(r) = n_0(1 + (r/r_c)^2)^{-3\beta/2}$.

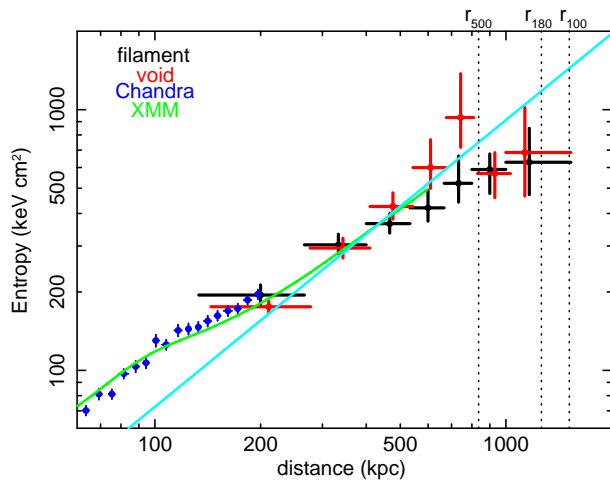


Fig. 6. Entropy profiles in the filament (black) and void (red) directions. Crosses and diamonds show entropy calculated from the resulting temperature and electron density, respectively, as shown in Figures 4 and 5. Chandra results (David et al. 2001) are represented by blue crosses. The green line shows the entropy profile calculated by combining the electron density from XMM and the temperature from Suzaku. The light blue line extrapolates the Suzaku and XMM data (green line) with a power-law formula fit for the data beyond 200 kpc, which has a fixed index of 1.1.

4.3. Entropy profiles

Entropy, which is a useful tool for investigating the thermodynamic history of hot gas in groups and clusters, is defined as

$$S = \frac{kT}{n_e^{2/3}}, \quad (1)$$

where T and n_e are the temperature and deprojected electron density, respectively. In Figure 6, we show the entropy profiles of the Hydra A cluster calculated from the derived temperature and electron density profiles shown in Figures 4 and 5. Entropy in the two directions increased from the center to 800 kpc, or r_{500} , which was derived from the Navarro, Frenk and White (NFW) model fit to the hydrostatic mass described in section 4.4. Between 500 kpc and 800 kpc, the entropy in the void direction was systematically higher than in the filament

direction. At the two outermost radial bins (beyond r_{500}), the entropies of the two directions agree well. In addition, we calculated the entropy profile by combining the parameters resulting from the fit of the electron density profile from XMM and the temperature profile from Suzaku as indicated by the green line in Figure 6. The entropy profiles using Suzaku, XMM, and Chandra data are consistent with each other (figure 6).

The derived entropy profiles were compared with a power-law model with a fixed index of 1.1, which was expected from simulations of the accretion shock heating model (Tozzi & Norman 2001; Ponman, Sanderson, Finoguenov 2003). From 200 kpc to 500 kpc, the derived entropy profiles agreed well with the $r^{1.1}$ relationship. In contrast, beyond 800 kpc, or $\sim r_{500}$, the entropy profiles in the two directions were systematically lower than the predicted by the $r^{1.1}$ relationship. Inside 200 kpc, the entropy exceeded the model prediction, which attribute to the presence of the cool core boundary (Peres et al. 1998) and the shock front around 200 kpc.

4.4. Hydrostatic mass

We estimated the hydrostatic or gravitational mass assuming the hydrostatic equilibrium given by,

$$M_{\text{H.E.}}(< r) = -\frac{kT(r)r}{\mu m_p G} \left(\frac{d \ln \rho(r)}{d \ln r} + \frac{d \ln kT(r)}{d \ln r} \right), \quad (2)$$

where $M_{\text{H.E.}}(< r)$ is the hydrostatic mass within the three-dimensional radius r , G is the gravitational constant, k is the Boltzmann constant, ρ is the gas density, kT is the temperature, and μm_p is the mean particle mass of the gas (the mean molecular weight is $\mu = 0.62$). Here, we assumed spherically symmetric mass distribution.

On the basis of the temperature and electron density profiles, we calculated the hydrostatic mass of the Hydra A cluster beyond 100 kpc. The temperature gradient of the i th shell was calculated from a power-law fit of temperatures of shells ($i-1$), i , and ($i+1$). We employed the electron density profile from the single- β model fit shown in table 5. The derived hydrostatic mass is plotted in Figure 7 as diamonds with the integrated gas mass profiles and stellar mass profiles derived in subsection 4.6. The derived mass was calculated for the whole azimuthal angle under the assumption of spherical symmetry

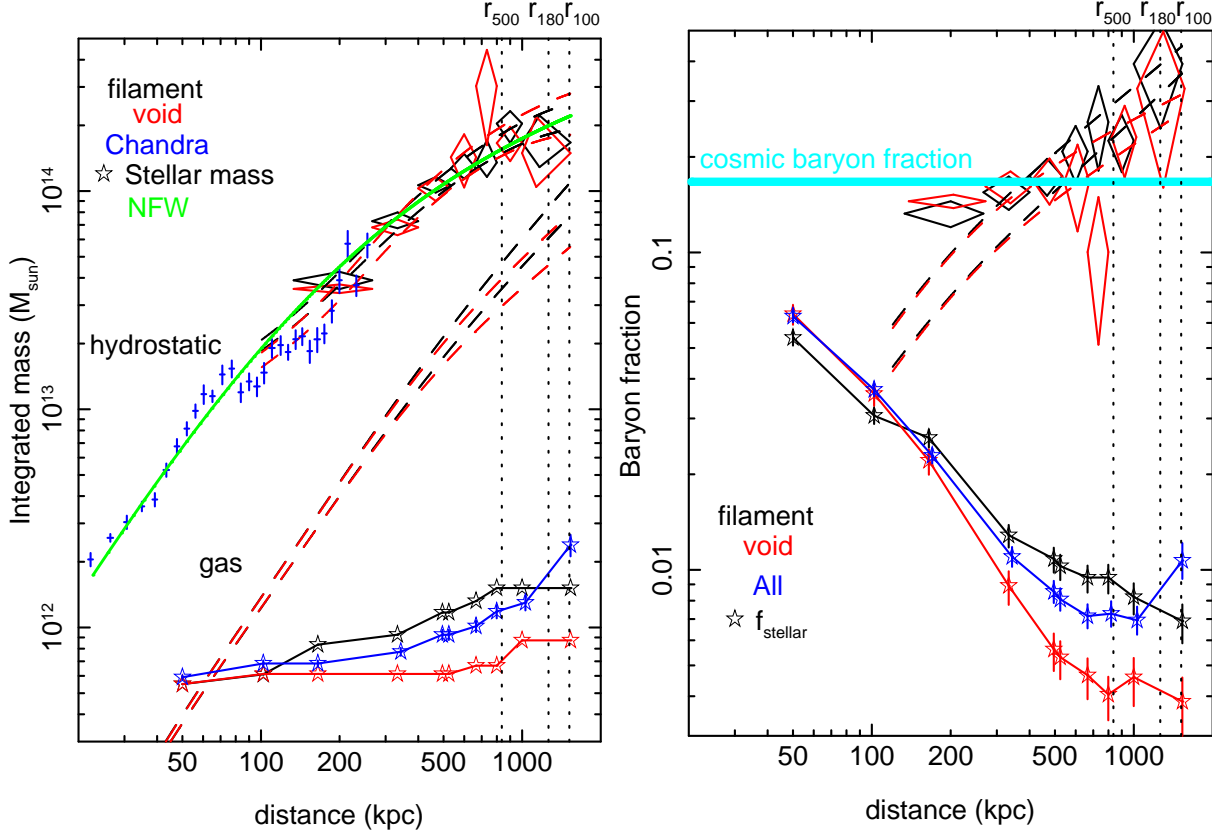


Fig. 7. left: Integrated hydrostatic and gas-mass profiles. All the black and red colors show the filament and void directions, respectively. The masses were calculated in the whole azimuthal angle under the assumption of spherical symmetry for each direction. The hydrostatic mass was calculated from the temperatures of shells ($i - 1$), i , and ($i + 1$) (diamonds) and the exponential relationship (dashed lines). All dashed lines show 90% upper and lower limits. The green line shows the best-fit NFW model. The integrated stellar mass profiles in the filament and void directions using 2MASS data are represented by stars. Blue stars are the integrated stellar mass profile in the whole azimuthal angle corrected for the contribution of the fainter galaxies using LF (solid). right: Cumulative profiles of gas fraction, $f_{\text{gas}}(< r)$ assuming hydrostatic equilibrium in both directions. The diamonds show $f_{\text{gas}}(< r)$ of the integrated hydrostatic and gas mass of the corresponding directions. Dashed lines represent $f_{\text{gas}}(< r)$ applying the result of the NFW model fit. The value of the cosmic baryon fraction (light blue) from WMAP (Komatsu et al. 2011) is plotted. The stars represent the stellar fraction, $f_{\text{star}}(< r)$, using the NFW model fit. The meanings of the colors and line styles are the same as in the left panel.

using the parameters derived for each direction: thus, the mass in each direction was four times larger than that in the corresponding direction. Although the electron density in the filament direction at a given radius was higher than that in the void direction, the difference in the slopes of the electron density was small. As a result, the hydrostatic masses derived for the two directions agree well. In addition, we calculated the 90% range of hydrostatic mass using the exponential relationship of the temperature profiles and fits of the electron-density profiles with the double- β model, which are plotted as dashed lines in Figure 7.

We fitted the derived hydrostatic mass profiles with the following NFW formula, which shows the equilibrium density profile of the dark matter halo (Navarro et al. 1996; Navarro et al. 1997);

$$M_{\text{NFW}}(< r) = 4\pi\delta_c\rho_c r_s^3 \left[\ln(1+x) - \frac{x}{1+x} \right], x \equiv r/r_s, (3)$$

where $M_{\text{NFW}}(< r)$ is the mass within a radius r , ρ_c is the critical baryon density of the Universe, r_s is the scaled radius, and δ_c is the characteristic density, that can be expressed in terms of the concentration parameter ($c = r_{200}/r_s$) as

$$\delta_c = \frac{200}{3} \frac{c^3}{\ln(1+c) - c/1+c}. (4)$$

Since the hydrostatic masses derived for the two directions agree well, we fitted the two hydrostatic mass profiles with Suzaku and that with Chandra simultaneously, excluding the shock region from 100 kpc to 200 kpc. The parameters derived from the fit are shown in Table 7. The quantity r_{100} is equal to r_{vir} in Hydra A cluster, since for our fiducial cosmological model, $\Delta_{\text{vir}} = 100$ for halos with a redshift $z = 0.0539$ (Nakamura & Suto 1997). We estimated r_{Δ} for various overdensities: $\Delta = 500, 200, 180$ and 100 , and r_{Δ} derived from fits with the NFW model are 811 ± 10 kpc, 1189 ± 96 kpc, 1243 ± 16 kpc, and 1577 ± 22 kpc, respectively. The r_{100} is close to the outermost ring radius. Possible deviations from hydrostatic equilibrium have been previously discussed to explain the entropy flattening beyond r_{500} (Bautz et al. 2009; George et al. 2009; Kawaharada et al. 2010): therefore, we fitted the hydrostatic mass out to r_{500} . We were able to obtain almost the same results as shown in Table 7. Thus, the NFW model represents the hydrostatic mass out to r_{100} within error bars as shown in Figure 7.

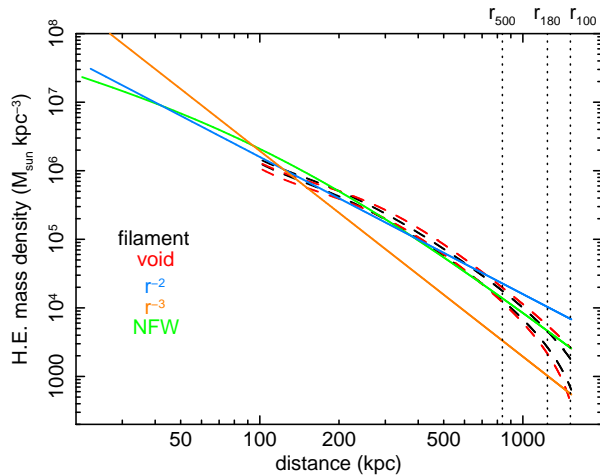


Fig. 8. H.E. mass density profiles for the filament (black) and void (red) directions. Density was calculated from the integrated H.E. mass profile. The r^{-2} and r^{-3} profiles are plotted with solid blue and orange lines, respectively.

Moreover, we calculated the total mass density profile from the total integrated hydrostatic mass profile in each direction. The density profile was also calculated from the NFW model obtained above. The calculated density profiles were compared with r^{-2} and r^{-3} profiles (Figure 8). The NFW density profile varied from r^{-1} to r^{-3} with increasing radius. Within r_{500} , the densities are well represented by the r^{-2} profile, which is shallower than the asymptotic matter density slope $\rho \propto r^{-3}$. Beyond r_{500} , the r^{-3} profile is preferable than the r^{-2} profile.

4.5. Gas fraction

We derived the cumulative gas mass fraction as,

$$f_{\text{gas}}(< r) = \frac{M_{\text{gas}}(< r)}{M_{\text{H.E.}}(< r)}, \quad (5)$$

where $M_{\text{gas}}(< r)$ and $M_{\text{H.E.}}(< r)$ are the gas mass and hydrostatic mass, respectively, within a sphere of radius r . As shown in Figure 7 and Table 6, the gas fraction increased in the outskirts and reached the cosmic mean baryon fraction derived from seven-year data of Wilkinson microwave anisotropy probe (WMAP7; Komatsu et al. 2011) at $\sim 0.5 r_{500}$. At r_{100} , $f_{\text{gas}}(< r)$ in the filament direction exceeded the result of WMAP7, while the lower limit of $f_{\text{gas}}(< r)$ in the void direction reached the WMAP 7 fraction. Adopting the fit of the NFW model to the hydrostatic mass resulted in $f_{\text{gas}}(< r)$ in the void and the filament directions at r_{100} , exceeding the cosmic baryon fraction by a factor of 2 and 3, respectively. Furthermore, $f_{\text{gas}}(< r)$ in the void direction at r_{180} was close to that derived for the north-west direction of the Perseus cluster at r_{200} (Simionescu et al. 2011): r_{180} was derived from the NFW model fit of the hydrostatic mass. The radial profile of $f_{\text{gas}}(< r)$ of the Abell 1246 cluster with $kT = 6.0$ keV exhibited similar behavior as that of our result of the Hydra A cluster (Sato et al. 2012).

4.6. K-band Luminosity of galaxies and stellar fraction

The ratio of gas mass to stellar luminosity is a key parameter for studying the star formation efficiency in clusters

of galaxies. Since almost all metals in the ICM are synthesized in galaxies, the metal-mass-to-light ratio provides a useful measure for studying the ICM chemical evolution. To estimate the gas-mass and Fe-mass-to-light ratios, we calculated the K -band luminosity of Hydra A cluster on the basis of the Two Micron All Sky Survey (2MASS) catalog, whereby all data is presented in a $2^\circ \times 2^\circ$ box: the coordinates of objects are shown in the left panel of Figure 9. The smoothed distribution of galaxies around Hydra A obtained from 2MASS is shown in the right panel of Figure 9. The distribution of galaxies is elongated in the filament direction toward the Abell 754 cluster, which exhibited a redshift close to that of Hydra A. In the void direction, the density of galaxies was significantly lower. Toward the south, an additional filament-like distribution of galaxies appeared from the Hydra A cluster. Hydra A itself was discovered to have an apparent magnitude of $m_K = 11.07$, or $L_K = 5 \times 10^{11} L_{K,\odot}$ using a luminosity distance $D_L = 240$ Mpc and a foreground Galactic extinction of $A_K = 0.015$ (Schlegel, Finkbeiner, Davis 1998). Among galaxies in the NED data base² with available redshifts, those with heliocentric velocities differ from that of the Hydra A cluster by >2000 km/s were excluded from the analysis. The K -band surface brightness profile centered on Hydra A is shown in figure 10. Beyond ~ 2000 kpc from the cluster center, the K -band surface brightness flattened. Therefore, we adopted the region between 2000 kpc and 4000 kpc as a background.

Figure 10 also shows the luminosity function (LF) of galaxies in the Hydra A cluster within r_{100} . Here, we used as background the LF of galaxies from 2000 kpc to 4000 kpc from the center of the Hydra A cluster. The completeness limit of galaxies of 2MASS is $K_s = 13.5$ in apparent magnitude³, which corresponds to the K -band luminosity, $L_K = 7 \times 10^{10} L_{K,\odot}$ for the distance of the Hydra A cluster. The total K -band luminosity of galaxies above the 2MASS complete limit and that of all the detected galaxies including those below the limit are $1.5 \times 10^{12} L_{K,\odot}$ and $2.5 \times 10^{12} L_{K,\odot}$, respectively. To calculate the total light of the cluster, we evaluate the contribution of fainter galaxies below the 2MASS limit. The LF of galaxies in clusters can be described with the Schechter function as,

$$\phi(L)dL = \phi_* \left(\frac{L}{L_*}\right)^\alpha \exp(-L/L_*) d\left(\frac{L}{L_*}\right) \quad (6)$$

where the parameters L_* , ϕ_* , and α are the characteristic luminosity, number densities, and faint-end power-law index, respectively. Upon adopting the L_* of stacked cluster galaxies by Lin, Mohr, Stanford (2003) and integrating the Schechter function below the 2MASS limit, the total K -band luminosity becomes $2.2 \times 10^{12} L_{K,\odot}$, which is smaller than that of all the galaxies detected by 2MASS including those below the complete limit. If we allow L_* to vary, the fit for the LF of the Hydra A cluster improves, as shown in Figure 10, and the total K -band luminosity becomes $2.8 \times 10^{12} L_{K,\odot}$. Therefore, the simple sum of K -band luminosities of the detected galaxies, including those below the 2MASS complete limit is close to that integrated luminosity of the Schechter function. Therefore, we adopted the total K -band luminosity

² <http://nedwww.ipac.caltech.edu/>

³ See <http://www.ipac.caltech.edu/2mass/releases/second/doc/explsum.html>

Table 6. Cumulative values of the hydrostatic mass ($M_{H.E.}$), gas mass (M_{gas}), and gas fraction (f_{gas}) of the Hydra Hydra A cluster.

Region r (kpc)	filament			void		
	M_{gas} ($10^{14} M_{\odot}$)	$M_{H.E.}$ ($10^{14} M_{\odot}$)	f_{gas}	M_{gas} ($10^{14} M_{\odot}$)	$M_{H.E.}$ ($10^{14} M_{\odot}$)	f_{gas}
133 – 266	0.052 ± 0.001	0.39 ± 0.04	0.13 ± 0.01	0.052 ± 0.001	0.36 ± 0.02	0.15 ± 0.01
266 – 400	0.11 ± 0.01	0.72 ± 0.07	0.15 ± 0.02	0.11 ± 0.01	0.68 ± 0.06	0.16 ± 0.02
400 – 533	0.19 ± 0.02	1.06 ± 0.09	0.17 ± 0.02	0.17 ± 0.02	1.03 ± 0.13	0.17 ± 0.03
533 – 666	0.26 ± 0.03	1.27 ± 0.21	0.21 ± 0.04	0.24 ± 0.03	1.43 ± 0.39	0.17 ± 0.05
666 – 799	0.35 ± 0.05	1.35 ± 0.35	0.26 ± 0.08	0.30 ± 0.04	3.03 ± 1.41	0.10 ± 0.05
799 – 997	0.46 ± 0.07	2.04 ± 0.37	0.22 ± 0.05	0.38 ± 0.06	1.66 ± 0.31	0.23 ± 0.06
997 – 1529	0.71 ± 0.12	1.82 ± 0.60	0.39 ± 0.14	0.55 ± 0.11	1.67 ± 0.78	0.33 ± 0.17

Table 7. Resulting radii r_c and r_{200} , and concentration parameter c_{200} derived from the NFW model.

	r_s (kpc)	r_{200} (kpc)	c
fitted up to r_{500}	126 ± 8	1189 ± 96	9.44 ± 0.48
fitted up to r_{100}	123 ± 8	1183 ± 98	9.62 ± 0.49

of $(2.5 \pm 0.3) \times 10^{12} L_{K,\odot}$.

We collected K -band luminosity of galaxies in the north-west and north-east sectors for the filament and void directions, respectively, as well as in the whole azimuthal angle and derived brightness profiles in the K -band. For the whole azimuthal angle, we collected galaxies above the 2MASS complete limit and evaluated the contribution of fainter galaxies by integrating the Schechter function. We obtained almost the same radial profile of K -band luminosity as that from the simple sum of luminosities of all the galaxies detected with 2MASS. Therefore, for the filament and void directions, we collected all the galaxies detected by 2MASS in each direction and derived radial profile of K -band luminosity. After subtracting the background, we deprojected the brightness profile of galaxies (under the assumption of spherical symmetry) and derived three-dimensional radial profiles of K -band luminosity in the filament, void, and whole azimuthal angle.

Figure 7 shows the integrated K -band luminosity profiles. As opposed to the integrated luminosity of the whole azimuthal angle, figure 7 uses the four-times luminosity of the filament and void directions. The filament direction shows a systematically higher K -band luminosity than that in void direction. The integrated K -band luminosity profiles of these two directions become flatter from ~ 800 -1000 kpc, and the contribution of galaxies beyond 1000 kpc is small. The integrated luminosity profile of the whole azimuthal angle is between those in the filament and void directions except for the outermost region around 1200 kpc (Figure 7 and 9). This result is attributed to the luminosity of the whole azimuthal angle being affected by the filamentary structure around 1200 kpc in the south of the Hydra-A cluster.

We derived cumulative stellar mass fraction as,

$$f_{\text{star}}(< r) = \frac{M_{\text{star}}(< r)}{M_{\text{H.E.}}(< r)} \quad (7)$$

where, $M_{\text{star}}(< r)$ is the total stellar mass within r , derived from the total K -band luminosity within r , under the assumption that the stellar-mass-to-light ratio in the K -band is unity (Nagino & Matsushita 2009). At a given radius, the $f_{\text{star}}(< r)$

in the filament direction is higher by a factor of 2–3 than that in the void direction, reflecting the concentration of galaxies in the filament direction (Figure 7). Beyond r_{500} , $f_{\text{star}}(< r)$ is smaller than $\sim 1\%$, and does not contribute to the baryon fraction. We also derived the stellar mass fraction using the whole azimuthal angle using the NFW mass for the filament and void directions. Although the stellar fraction continues to decrease with radius in the filament and the void directions, the stellar fraction in whole azimuthal directions shows a minimum at $\sim r_{500}$, and increases with radius by a factor of ~ 1.5 from r_{500} to r_{100} .

Using the integrated K -band luminosity profile, we calculated the gas-mass-to-light ratio in the filament and void directions (Figure 11). The radial profile of the gas-mass-to-light ratio in the two directions increased with radius out to r_{100} . We also calculated the gas-mass-to-light ratio in the whole azimuthal angle, using the stellar luminosity in the whole azimuthal angle and the gas mass in the void direction which agrees that for the whole azimuthal angle derived by ROSAT (Ikebe et al. 1997).

5. Discussions

The Hydra A cluster is the first medium-sized cluster observed with Suzaku out to the virial radius. Suzaku observed the northern half of the cluster, and we derived radial profiles of temperature, electron density, entropy, hydrostatic mass, and K -band stellar luminosity in the filament and void directions. Temperature and entropy carry important information about the thermal history of the ICM. In subsection 5.1, we compare these profiles of the Hydra A cluster and other clusters observed with Suzaku and XMM to study their dependence on the system mass or on average ICM temperature. Next, we discuss possible explanations for entropy flattening and the higher gas-mass-to-hydrostatic-mass ratio at cluster outskirts. Discrepancies between electron and ion temperatures are discussed in subsection 5.2, deviations from hydrostatic equilibrium and the gas-clumping effect are discussed in subsections 5.3 and 5.4. We also derive IMLR of the Hydra A cluster out

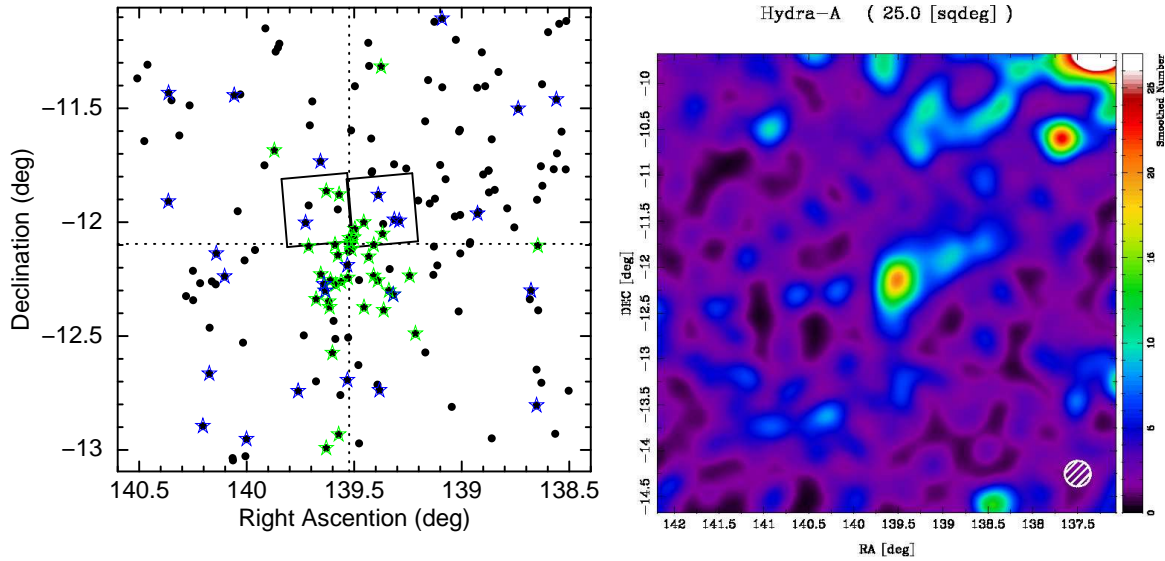


Fig. 9. Two-dimensional density distributions of galaxies around Hydra A, retrieved from 2MASS in the K -band. left: Stars represent galaxies with available redshift in the NASA/IPAC Extragalactic Database (NED). Green and blue stars indicate members and non-members, respectively, of the Hydra A cluster based on their redshift. The boxes represent the Suzaku fields of view (FOVs) of XIS pointings. The directions of the filament (north-west) and the void (north-east) are separated as dashed lines. Right: The box size is $5^\circ \times 5^\circ$. Abell 754 cluster, with coordinates (RA, Dec) = (137.2087, -9.6366) in degrees, is shown in top right. A Gaussian smoothing scale is represented by the white hatched circle at bottom right.

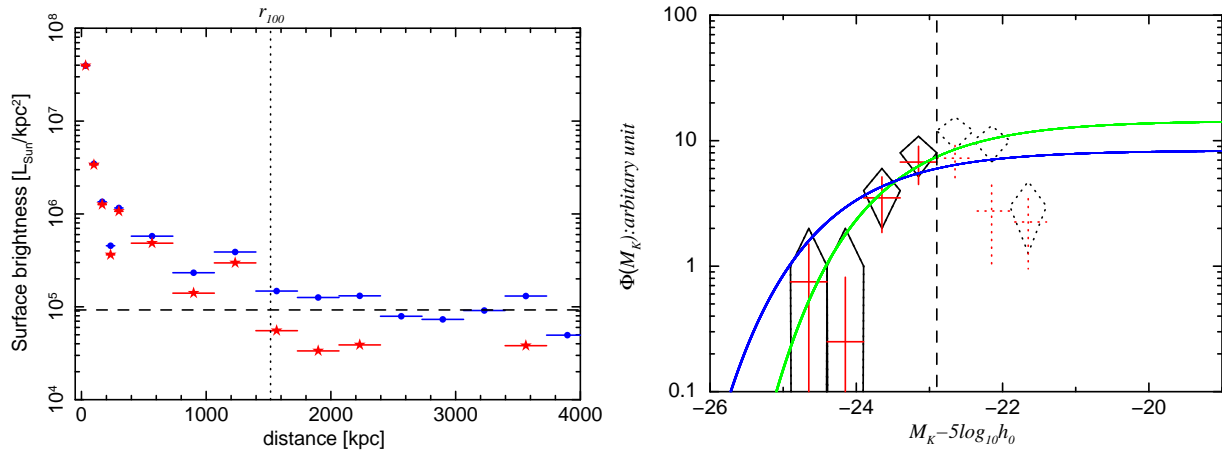


Fig. 10. left: Surface-brightness profile of Hydra A observed with 2MASS photometric data in the K -band. Blue points denote the detected galaxies of Hydra A and red stars denote the background-subtracted data. The dashed line shows the subtracted background level and the dotted line shows r_{100} . right: The LF of Hydra A observed with 2MASS photometric data in the K -band within r_{100} in absolute magnitude form, including background galaxies (black diamonds) and that the subtracted background contribution (red crosses). The vertical dashed line represents the complete limit of 2MASS. Blue and green solid lines show the best-fit Schechter functions when L_* was fixed to the result from the stacked LF of galaxies in clusters by Lin, Mohr, Stanford (2003) and allowed to vary, respectively.

to the virial radius in subsection 5.5 to constrain the star formation history in the cluster.

5.1. Comparison of temperature and entropy profiles with other systems

Figure 12 compares the temperature profiles of the Hydra A cluster and several clusters observed with Suzaku, scaled with average temperature, $\langle kT \rangle$, and r_{200} . Here, $r_{200} = 2.77 h_{70}^{-1} \sqrt{\langle kT \rangle / 10 \text{ keV}} / E(z)$ Mpc, with $E(z) = (\Omega_M(1+z)^3 + 1 - \Omega_M)^{1/2}$ (Henry et al. 2009). Then, r_{200} of the Hydra A cluster is 1.48 Mpc. Within $0.5r_{200}$, the temperature profiles agree with the scaled temperature relationship by Pratt et al.

(2007), which is derived from a sample of 15 clusters observed with XMM out to $\sim r_{500}$. In contrast, beyond $0.5r_{200}$, the observed temperatures scatter by a factor of two, and tend to be lower than the XMM relationship. In the scaled temperature profiles, there was no evidence of any significant dependence on the average ICM temperature, or system mass. Some variation in the temperature profiles should reflect the azimuthal variation as observed in Abell 1689 (Kawaharada et al. 2010) and Abell 1246 (Sato et al. 2012).

In figure 13, we compare the entropy profile of the Hydra A cluster with other clusters observed with Suzaku; these profiles are scaled with the average ICM temperature and r_{200} by

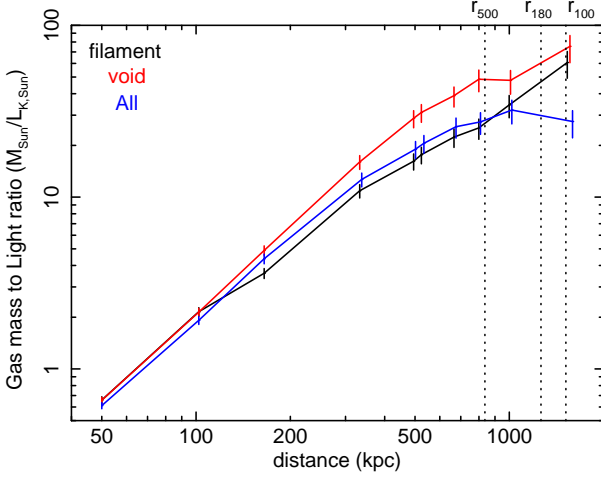


Fig. 11. Cumulative gas-mass-to-light ratio M_{gas}/L_K in the filament (black) and void (red) directions and for the whole azimuthal angle (blue).

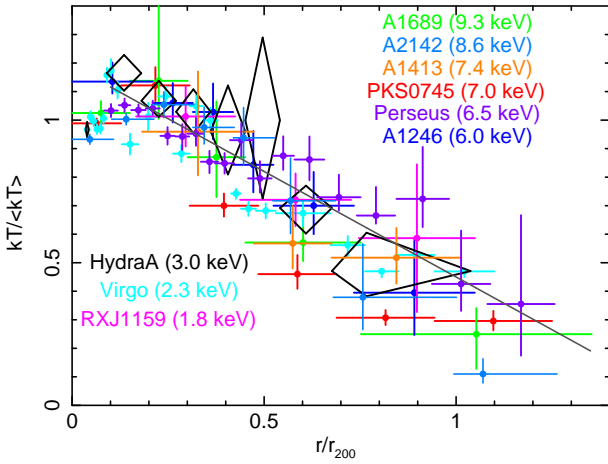


Fig. 12. Radial profiles of temperature of clusters observed with Suzaku and XMM. Here, the temperature profiles are scaled with the average ICM temperature, $\langle kT \rangle$, and are azimuthally averaged. We plotted the radial profiles of cluster of galaxies Abell 1689 (Kawaharada et al. 2010), Abell 2142 (Akamatsu et al. 2011), Abell 1413 (Hoshino et al. 2010), PKS-0745 (George et al. 2009), the Perseus cluster (Simionescu et al. 2011), Abell 1246 (Sato et al. 2012), the Virgo cluster (Urban et al. 2011), RXJ1159 (Humphrey et al. 2011) and the Hydra A cluster (current study). The scaling radius r_{200} was calculated by Henry et al. (2009). The solid line represents the scaled temperature profile by Pratt et al. (2007).

Henry et al. (2009). Here, we used the weighted average of the radial profiles of different directions of each cluster. Contrary to the expected $r^{1.1}$ relationship, these profiles become flat beyond $0.5r_{200}$. Except for PKS-0745 (George et al. 2009), the scaled entropy profiles of these clusters were universal with ICM temperatures above 3 keV and did not depend on the ICM temperature. For the PKS-0745 cluster, Eckert et al. (2011) determined that the ROSAT surface-brightness profile is statistically inconsistent (7.7σ) with Suzaku results beyond r_{200} and that the difference is likely explained by the existence of additional foreground components at the low Galactic latitude of the source. These components were not considered in the

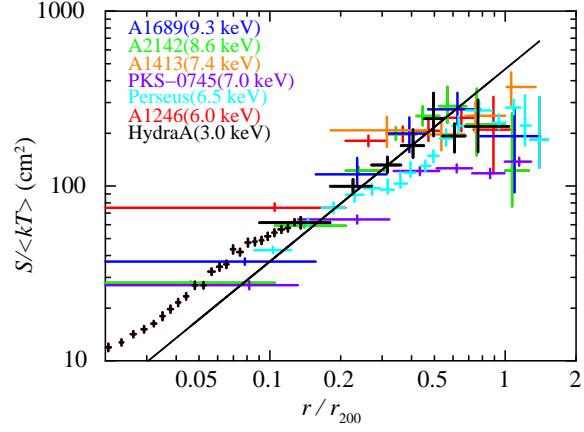


Fig. 13. Radial profiles of entropy of cluster observed with Suzaku and scaled: with the average ICM temperature, $\langle kT \rangle$, and are azimuthally averaged. Data for Abell 1689 (Kawaharada et al. 2010) are plotted in dark blue, for Abell 2142 (Akamatsu et al. 2011) in green, for Abell 1413 (Hoshino et al. 2010) in orange, for PKS-0745 (George et al. 2009) in purple, for Perseus (Simionescu et al. 2011) in light blue, for Abell 1246 (Sato et al. 2012) in red, and for Hydra A (current study) in black. The scaling radius r_{200} was calculated by Henry et al. (2009). The solid line shows the power-law profile with slope of 1.1. The normalization of the power-law is scaled with our result for the Hydra A cluster.

Suzaku background modeling.

5.2. Ion-electron relaxation in the Hydra A cluster

One interpretation for the flattening of the entropy profile is that caused by deviations in electron and ion temperatures (Hoshino et al. 2010; Akamatsu et al. 2011). The time-scale for thermal equilibration between electrons and ions through Coulomb scattering is given by

$$t_{ei} \sim 0.14 \left(\frac{n_e}{10^{-4} \text{ cm}^{-3}} \right)^{-1} \left(\frac{kT}{1.5 \text{ keV}} \right)^{3/2} \text{ Gyr} \quad (8)$$

(Takizawa & Mineshige 1998; Takizawa 1998; Takizawa 1999; Akahori & Yoshikawa 2010). Considering this time-scale and the shock propagation speed, the radial length above which the electron temperature is significantly lower than the ion temperature is proportional to the square of the ICM temperature (Takizawa 1999). On the other hand, r_{200} is proportional to the square root of the ICM temperature. Therefore, some dependence on the mean ICM temperature is expected in the temperature and entropy profiles. However, there is no systematic dependence on the average ICM temperature in the temperature and entropy profiles, as shown in figure 12 and figure 13. Furthermore, if the ICM temperature is underestimated and the actual entropy profile of the Hydra A cluster follows the $r^{1.1}$ relationship, a flat ICM temperature profile is necessary, i.e., $r \sim 0$ out to r_{100} , considering the electron density profile of $r^{-(1.6 \sim 1.7)}$ beyond 400 kpc. However, the flat temperature profile contradicts to the results of numerical hydrodynamical simulations, where negative gradients of the temperature profiles outside cool core regions are naturally produced (Borgani et al. 2002; Burns et al. 2010; Nagai & Lau 2011). Therefore, for the Hydra A cluster, it is difficult to explain the flattening of the observed entropy profiles by deviations of ion-electron

temperatures.

5.3. Deviations from hydrostatic equilibrium

The remaining interpretation for the flattening of the entropy profiles at the cluster outskirts is deviations from hydrostatic equilibrium, because when the gas-clumping effect is significant, we also expect that the ICM also deviates from hydrostatic equilibrium. Then, infalling matter may have retained some of its kinetic energy in the form of bulk motions, and the thermal energy deficit in the ICM yields lower entropy. Furthermore, the underestimate of the gravitational mass and/or gas clumping leads to an overestimation of the baryon fraction. Recent numerical simulations by Vazza et al. (2009) and Nagai, Vikhlinin, Kravtsov (2007) have shown that the kinetic energy of bulk motion carries $\sim 30\%$ of the total energy around the virial radius. With simulations, Nagai & Lau (2011) showed that beyond r_{200} , gas clumping leads to an overestimation of the observed gas density and causes flattening of the entropy profile. If the hydrostatic mass was underestimated by 130% in the filament direction and 100% in the void direction, the baryon fractions at r_{100} would have the same value as that of WMAP7, although the observed gas fraction calculated from the hydrostatic mass in the void direction is consistent with the WMAP7 result within error bars.

The distributions of the ICM and galaxies in the Hydra A cluster elongate in the filament direction. If the ICM is under hydrostatic equilibrium in a non-spherical dark matter halo, the X-ray emission and dark matter halo elongate in the same direction. Numerical simulations by Burns et al. (2010) determined that gas, galaxies, and dark matter continue in the filament direction due to the accretion of gas and subclusters. Then, it is reasonable that the dark matter halo also elongates in the filament direction. However, the hydrostatic mass in the void and filament directions of the Hydra A cluster are in good agreement. These results indicate that deviations from hydrostatic equilibrium should be more significant in the filament direction than in the void direction.

The clumping effect will also be higher in the filament direction, since smaller systems are thought to be accreted from this direction. For the Hydra A cluster, we were not able to detect clump candidates with Suzaku. The spectra of detected point sources are consistent with those of background active galactic nuclei. Considering the luminosities of detected point sources, the luminosity of clumps should be smaller than a few 10^{41} erg s $^{-1}$, which corresponds to cores of groups of galaxies. Therefore, if clumps are significant, their scales should be smaller than those of small groups of galaxies.

5.4. The concentration-mass relationship

From numerical simulations, a weak variation in the concentration is expected from low-mass to high-mass clusters, reflecting differences in the formation epochs of low-mass and high-mass halos (Navarro et al. 1997; Bullock et al. 2001; Dolag et al. 2004). Pointecouteau, Arnaud, Pratt (2005), Ettori et al. (2011) and Okabe et al. (2010) investigated the relationship between the concentration parameter and the cluster mass, or the concentration-mass ($c - M$) relationship. The results are compatible with the intrinsic dispersion of theoretical predictions. Figure 14 compares the $c - M$ relationship of the

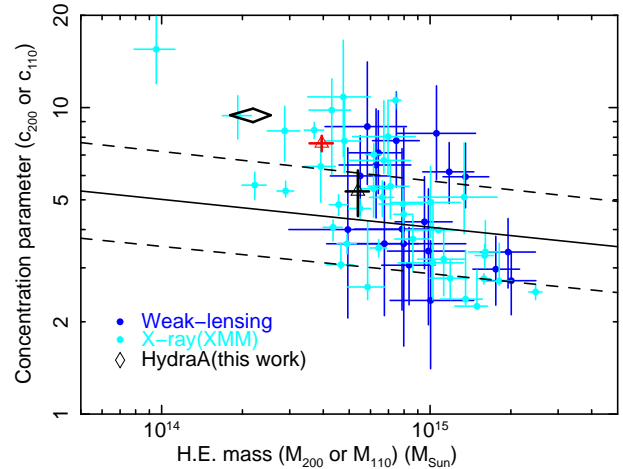


Fig. 14. Observed distribution of concentration parameters as a function of cluster masses. The mass of weak lensing (blue) and X-ray (light blue) were defined by Okabe et al. (2010) and Ettori et al. (2010);Ettori et al. (2011), respectively. Okabe et al. (2010) used M_{110} and c_{110} , while Ettori et al. (2010);Ettori et al. (2011) used M_{200} and c_{200} . We considered M_{100} for Hydra A. The solid line indicates the median relationship determined through CDM simulations for the WMAP5 cosmological model, while the region enclosed within the dashed lines corresponds to the range of $\sigma(\log_{10} c) = 0.1$, within which most of simulated clusters are distributed (Duffy et al. 2008). The large diamond shows the observed mass profile of Hydra A (current work) assuming hydrostatic equilibrium. Black and red open triangles correspond to cases in which the $f_{\text{gas}}(< r)$ value of Hydra A (current work) is the same as the cosmic mean baryon fraction (Komatsu et al. 2011) in the filament and the void directions, respectively.

Hydra A cluster and other clusters observed with weak-lensing (Okabe et al. 2010), and clusters observed with XMM by Ettori et al. (2011). An assumption of cluster dynamical state or hydrostatic equilibrium is not required in the weak-lensing results. The distribution of the $c - M$ relationship of these clusters agrees well with the relation expected from the numerical simulations by Duffy et al. (2008), although Ettori et al. (2011) found that relatively low-mass systems tend to have higher concentration parameters.

The hydrostatic mass in the Hydra A cluster of the filament and void directions are represented with the same NFW mass model with $c_{\text{vir}} = 9 - 10$ and $M_{\text{vir}} = (2.2 \pm 0.4) \times 10^{14} M_{\odot}$. As shown in Figure 14, this $c_{\text{vir}} - M_{\text{vir}}$ relationship of the Hydra A cluster was outside $\sigma(\log_{10} c) = 0.1$ within which most clusters from numerical simulations are distributed Duffy et al. (2008). If the hydrostatic mass was underestimated and the baryon fraction using the gravitational mass beyond r_{500} of the Hydra A cluster is the same as the cosmic mean baryon fraction in the two observed directions, the fits with the NFW model yielded smaller values of c_{vir} and higher values M_{vir} as shown in Figure 14. In this case, the derived value of M_{vir} in the filament direction became higher than that in the void direction. This result also indicates that the ICM in the outskirts of Hydra A deviates from hydrostatic equilibrium, and the X-ray emission and dark matter halo elongate in the same direction.

5.5. Metal-Mass-to-Light Ratios out to the virial radius

We derived integrated IMLR, mass-to-light ratio for Fe, out to the virial radius for the first time. Here, we show the IMLR

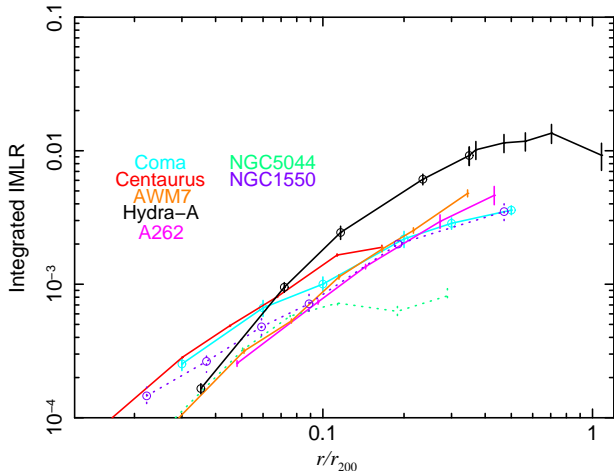


Fig. 15. Comparison of iron-mass-to-light-ratio for other clusters. The radius is scaled with the characteristic radius r_{200} (Henry et al. 2009). For comparison, we plotted the radial profile of cluster of galaxies AWM 7 (Sato et al. 2008, Sato et al. in preparation), Abell 262 (Sato et al. 2009b), the Centaurus cluster (Sakuma et al. 2011) and the Coma cluster (Matsushita et al. 2011) and galaxy groups NGC 5044 (Komiya et al. 2009) and NGC 1550 (Sato et al. 2010). Open circles are the result from XMM-Newton satellite, and others are Suzaku satellite.

profile for the whole azimuthal angle to compare other clusters observed with Suzaku. Within $0.3 r_{200}$ and beyond $0.3 r_{200}$, we used the Fe abundances obtained by Matsushita (2011) and this work, respectively. Here, within $8'–15'$, or $0.35–0.65 r_{200}$, we used the weighted average of the Fe abundance at the three radial bins in this region. The error bars of the mass-to-light ratio include the errors in both the abundance and the K-band luminosity caused by the uncertainty in the contribution of fainter galaxies below the 2MASS threshold (see section 5.5 for details). Figure 15 shows the cumulative IMLR profile of the Hydra A cluster. The IMLR profile increases with radius within $0.4–0.5 r_{200}$, and becomes flatter beyond $0.5 r_{200}$ with the value of $\sim 0.01 M_{\odot}/L_{K,\odot}$, which reflects the flattening of the gas-mass-to-light ratio beyond r_{500} . For the void and filament directions, the IMLR profiles should increase with radius beyond r_{500} .

At r_{200} , the cumulative IMLR was $0.007–0.01 M_{\odot}/L_{K,\odot}$. A previously reported theoretical model predicts that the oxygen-mass-to-light ratio (OMLR) of a cluster is a sensitive function of the slope of the initial mass function (IMF) (Renzini 2005). Here, the oxygen mass is a sum of that trapped in stars and that in the ICM. By adopting a Salpeter IMF with a slope of 2.35, the expected value of the OMLR is $\sim 0.1 M_{\odot}/L_{B,\odot}$. In contrast, a top-heavy IMF with a slope of 1.35 overproduces metals more than that with a factor of 20. For the Hydra A cluster, by adopting the ratio of stellar-mass-to-light ratio 4–6 in the B-band and K-band (Nagino & Matsushita 2009; Matsushita et al. 2011), the IMLR in the B-band becomes $0.03–0.06 M_{\odot}/L_{B,\odot}$ and the cumulative OMLR within the virial radius becomes $\sim 0.1–0.3 (A_{\text{O}}/A_{\text{Fe}}) M_{\odot}/L_{B,\odot}$. Here, A_{O} and A_{Fe} are abundances of O and Fe in solar units, respectively. Beyond r_{500} of the Hydra A cluster, the integrated stellar mass is only several percent of the integrated gas mass. Thus, even by considering the differ-

ence of stellar metallicity and the abundance of the ICM, most of the metals in the cluster are in the ICM. Therefore, for cases with solar O/Fe ratio, the OMLR is similar to the expectations reported by Renzini (2005), assuming a Salpeter IMF in the Hydra A cluster. In contrast, by adopting the O/Fe ratio from a nucleosynthesis model of SN II with metallicity = 0.02, as reported by Nomoto et al. (2006), the OMLR within the virial radius becomes $0.3–1.0 M_{\odot}/L_{B,\odot}$ in the Hydra A cluster. This value is larger than the expectation from the Salpeter IMF, and is consistent with a flatter IMF slope.

In Figure 15, the cumulative IMLR profile of the Hydra A cluster was compared with those of other groups and clusters, including Coma (8 keV; Matsushita et al. 2011), Centaurus (4 keV; Sakuma et al. 2011), and AWM 7 clusters (3.6 keV; Sato et al. 2008), as well as NGC 1550 (1.2 keV; Sato et al. 2010) and NGC 5044 groups (1.0 keV; Komiya et al. 2009). Within $0.5 r_{200}$, the cumulative IMLR profile of the Hydra A cluster increased with radius by a factor of two higher than for other systems. No systematic dependence on the ICM temperature was evident for clusters with temperatures higher than 2 keV, although beyond $0.1 r_{200}$, a group of galaxies shows a significantly smaller IMLR.

The stellar and gas-mass fractions within r_{500} depend on the total system mass (Lin, Mohr, Stanford 2003; Lin & Mohr 2004; Vikhlinin et al. 2006; Sun et al. 2009; Giodini et al. 2009). These studies determined that within r_{500} the stellar-to-total-mass ratios of the groups are much larger than those in the clusters, whereas the gas-mass fraction increases with the system mass. The observed higher stellar mass fraction and the lower gas mass fraction within r_{500} in poor systems are occasionally interpreted as proof that the star formation efficiency depends on the system mass. However, as shown in Figure 11, the gas is more extended than the stars in a cluster within r_{500} . The gas density profiles in the central regions of groups and poor clusters were observed to be shallower than those in the self-similar model, and the relative entropy level was correspondingly higher than that in rich clusters (Ponman, Cannon, Navarro 1999; Ponman, Sanderson, Finoguenov 2003; Sun et al. 2009). Then, the difference in the ratio of gas-mass-to-stellar-mass may reflect differences in distributions of gas and stars, which in turn reflects the history of energy injection from galaxies to the ICM. To study the fractions of stars and gas in clusters of galaxies, and its dependence on the system mass, we need measurements of gas and stellar mass beyond r_{500} of other clusters.

6. Summary and Conclusion

We presented the results of the Suzaku observation of the Hydra A galaxy cluster, which is the first medium-sized cluster (temperature ~ 3 keV) observed with Suzaku out to the virial radius. Two observations were conducted, north-west and north-east offsets, which continue in a filament direction and a void direction of the large-scale structure of the Universe, respectively. We investigated possible azimuthal variations in temperature, electron density, entropy and total mass profiles. Our analysis revealed that distributions of X-ray emission and galaxies elongate in the filament direction. The entropy profiles become flatter beyond r_{500} in contrast to the

$r^{1.1}$ relationship expected from the shock heating model of the ICM. The entropy profiles are universal in clusters observed with Suzaku when scaled with the averaged temperature of each cluster. The hydrostatic masses in the two directions agree and the NFW universal matter profile represents the hydrostatic mass distribution obtained up to $1.8 r_{500}$, with $c_{\text{vir}} = 9 - 10$ and $M_{\text{vir}} = (2.2 \pm 0.4) \times 10^{14} M_{\odot}$. The gas fraction, $M_{\text{gas}}(< r)/M_{\text{H.E.}}(< r)$ significantly exceeds the cosmic mean baryon fraction of WMAP7 beyond $\sim r_{500}$. The flattening of the entropy profile and higher gas fraction contradict expectations based on numerical simulations. An underestimate of gas temperature due to the discrepancy between ion and electron temperatures gives higher entropy and smaller gas fraction at cluster outskirts. However, a flat or increasing temperature profile is required. If bulk motions caused by infalling matter from filaments of clusters are higher than that of numerical simulations, and if the ICM deviates from the hydrostatic equilibrium, the entropy becomes smaller and the gas fraction is overestimated. In addition, we obtained IMLR up to the virial radius for the first time, and compared our results with other clusters and groups. The IMLR profile is consistent within $0.5 r_{200}$ with other clusters, and become flatter from $0.5 r_{200}$ to r_{200} .

References

- Anders, E., & Grevesse, N., 1989, *Geochim. Cosmochim. Acta*, 53, 197
- Akahori, T., & Yoshikawa, K. 2010, *PASJ*, 62, 335
- Akamatsu, H., Hoshino, A., Ishisaki, Y., et al. 2011, *PASJ*, 63, 1019
- Balogh, M. L., Christlein, D., Zabludoff, A. I., & Zaritsky, D. 2001, *ApJ*, 557, 117
- Bautz, M. W., et al. 2009, *PASJ*, 61, 1117
- Borgani, S., Governato, F., Wadsley, J., et al. 2002, *MNRAS*, 336, 409
- Bullock, J. S., Kolatt, T. S., Sigad, Y., Somerville, R. S., Kravtsov, A. V., Klypin, A. A., Primack, J. R., & Dekel, A. 2001, *MNRAS*, 321, 559
- Burns, J. O., Skillman, S. W., & O’Shea, B. W., 2010, *ApJ*, 721, 1105
- David, L. P., et al. 2001, *ApJ*, 557, 546
- Dolag, K., Bartelmann, M., Perrotta, F., Baccigalupi, C., Moscardini, L., Meneghetti, & M., Tormen, G. 2004, *A&A*, 416, 853
- Duffy, A. R., Schaye, J., Kay, S. T., & Dalla Vecchia, C. 2008, *MNRAS*, 390, L64
- Eckert, D., Molendi, S., Gastaldello, F., & Rossetti, M. 2011, *A&A*, 529, A133
- Ettori, S., Gastaldello, F., Leccardi, A., et al. 2010, *A&A*, 524, A68
- Ettori, S., Gastaldello, F., Leccardi, A., Molendi, S., Rossetti, M., Buote, D., & Meneghetti, M. 2011, *A&A*, 526, 1
- Evrard, August E., Metzler, Christopher A. & Navarro, Julio F. 1996, *ApJ*, 469, 494
- Finoguenov, A., Arnaud, M. & David, L. P. 2001, *ApJ*, 555, 191
- Fukazawa, Y., Makishima, K., Tamura, T., Nakazawa, K., Ezawa, H., Ikebe, Y., Kikuchi, K. & Ohashi, T. 2000, *MNRAS*, 313, 21
- Fujita, Y., Tawa, N., Hayashida, K., et al. 2008, *PASJ*, 60, 343
- George, M. R., et al. 2009, *MNRAS*, 395, 657
- Giodini, S., et al. 2009, *ApJ*, 703, 982
- Gitti, M., Nulsen, P. E. J., David, L. P., McNamara, & B. R., Wise, M. W. 2011, *ApJ*, 732, 13
- Gonzalez, A. H., Zaritsky, D., & Zabludoff, A. I. 2007, *ApJ*, 666, 147
- Henry, J. P., Evrard, A. E., Hoekstra, H., Babul, A., & Mahdavi, A. 2009, *ApJ*, 691, 1307
- Hoshino, A., et al. 2010, *PASJ*, 62, 371
- Humphrey, P. J., Buote, D. A., Brighenti, F., et al. 2011, arXiv:1106.3322
- Ikebe, Y., Makishima, K., Ezawa, H., et al. 1997, *ApJ*, 481, 660
- Ishisaki, Y., et al. 2007, *PASJ*, 59, 113
- Kalberla, P. M. W., Burton, W. B., Hartmann, D., Arnal, E. M., Bajaja, E., Morras, R., & Pöppel, W. G. L. 2005, *A&A*, 440, 775
- Kawahara, H. 2010, *ApJ*, 719, 1926
- Kawaharada, M., et al. 2010, *ApJ*, 714, 423
- Kaiser, N. 1991, *ApJ*, 383, 104
- Katayama, H., Takahashi, I., Ikebe, Y., Matsushita, K., & Freyberg, M. J. 2004, *A&A*, 414, 767
- Kirkpatrick, C. C., Gitti, M., Cavagnolo, K. W., McNamara, B. R., David, L. P., Nulsen, P. E. J., & Wise, M. W. 2009, *ApJ*, 707, L69
- Komatsu, E., et al. 2011, *ApJ*, S192, 18
- Komiyama, M., Sato, K., Nagino, R., Ohashi, T. & Matsushita, K. 2009, *PASJ*, 61, 337
- Koyama, K., et al. 2007, *PASJ*, 59, 23
- Kushino, A., Ishisaki, Y., Morita, U., Yamasaki, N. Y., Ishida, M., Ohashi, T., & Ueda, Y. 2002, *PASJ*, 54, 327
- Lane, W. M., Clarke, T. E., Taylor, G. B., Perley, R. A., & Kassim, N. E. 2004, *AJ*, 127, 48
- Leccardi, A. & Molendi, S. 2008, *A&A*, 487, 461
- Lin, Y.-T., Mohr, J. J., & Stanford, S. A. 2003, *ApJ*, 591, 749
- Lin, L. T., & Mohr, J., J. 2004, *ApJ*, 617, 879
- Lodders, K. 2003, *ApJ*, 591, 1220
- Makishima, K. et al. 2001, *PASJ*, 53, 401
- Markevitch, M., Forman, W. R., Sarazin, C. L. & Vikhlinin, A. 1998, *ApJ*, 503, 77
- Matsushita, K. et al. 2007a, *PASJ*, 59, 327
- Matsushita, K. 2011, *A&A*, 527, A134
- Matsushita, K., Sato, T., Sakuma, E., & Sato, K., submitted to *PASJ*
- Maughan, B. J. et al. 2008, *MNRAS*, 387, 998
- McNamara, B. R. et al. 2000, *ApJ*, 534, L138
- Mitsuda, K., et al. 2007, *PASJ*, 59, 1
- Molnar, S. M., et al. 2009, *ApJ*, 696, 1640
- Myrium, G., et al. 2011, *ApJ*, 732, 13
- Nagai, D., & Lau, E. T. 2011, *ApJ*, 731, 10
- Nagai, D., Vikhlinin, A., & Kravtsov, A. V. 2007, *ApJ*, 655, 98
- Nagino, R., & Matsushita, K. 2009, *A&A*, 501, 157
- Nakamura, T. T., & Suto, Y. 1997, *Prog. Theor. Phys.* 97, 49
- Navarro, J. F., Frenk, C. S., & White, S. D. M. 1996, *ApJ*, 462, 563
- Navarro, J. F., Frenk, C. S., & White, S. D. M. 1997, *ApJ*, 490, 493
- Nomoto, K., Tominaga, N., Umeda, H., Kobayashi, C., & Maeda, K. 2006, *Nuclear Physics A*, 777, 424
- Nulsen, P. E. J., David, L. P., McNamara, B. R., Jones, C., Forman, W. R., & Wise, M. W. 2002, *ApJ*, 568, 163
- Nulsen, P. E. J., McNamara, B. R., Wise, M. W., & David, L. P. 2005, *ApJ*, 628, 629
- Okabe, N., et al. 2010, *PASJ*, 60, 1133
- Peres, C. B., Fabian, A. C., Edge, A. C., Allen, S. W., Johnstone, R. M., & White, D. A. 1998, *MNRAS*, 298, 416
- Pratt, G. W., Böhringer, H., Croston, J. H., Arnaud, M., Borgani, S., Finoguenov, A., & Temple, R. F. 2007, *A&A*, 461, 71
- Pointecouteau, E., Arnaud, M., & Pratt, G. W. 2005, *A&A*, 435, 1
- Ponman, T. J., Cannon, D. B., & Navarro, J. F. 1999, *Nature*, 397, 135
- Ponman, T. J., Sanderson, A. J. R., & Finoguenov, A. 2003, *MNRAS*, 343, 331
- Reiprich, T. H., et al. 2009, *A&A*, 501, 899
- Renzini, A. 2005, *The Initial Mass Function 50 Years Later*, Edited by E. Corbelli and F. Palle, INAF Osservatorio Astrofisico di Arcetri, Firenze, Italy; H. Zinnecker, Astrophysikalisches Potsdam, Germany. *Astrophysics and Space Science Library* Volume 327. Published by Springer, Dordrecht, 2005, p.221
- Ryu, D., et al. 2003, *ApJ*, 593, 599

- Sakuma, E., Ota, N., Sato, K., Sato, T., & Matsushita, K. 2011, PASJ, 63, 979
- Sato, K. et al. 2007, PASJ, 59, 299
- Sato, K., Matsushita, K., Ishisaki, Y., Yamasaki, N. Y., Ishida, M., Sasaki, S. & Ohashi, T. 2008, PASJ, 60, 333
- Sato, K., Matsushita, K., Ishisaki, Y., Yamasaki, N. Y., Ishida, M. & Ohashi, T. 2009a, PASJ, 61, 353
- Sato, K., Matsushita, K. & Gastaldello, F. 2009b, PASJ, 61, 365
- Sato, K., Kawaharada, M., Nakazawa, K., Matsushita, K., Ishisaki, Y., Yamasaki, N. Y. & Ohashi, T. 2010, PASJ, 62, 1445
- Sato, T., Matsushita, K., Ota, N., Sato, K., Nakazawa, K. & Sarazin, C. L. 2011, PASJ, 63, 991
- Sato K., Matsushita, K., Yamasaki, N. Y., Sasaki, S., & Ohashi, T., submitted to PASJ
- Schelegel, D. J., Finkbeiner, D. P., & Davis, M. 1998, ApJ, 500, 525
- Simionescu, A., Werner, N., Böhringer, H., Kaastra, J. S., Finoguenov, A., Brüggén, M. & Nulsen, P. E. J. 2009, A&A, 493, 409
- Simionescu, A., Roediger, E., Nulsen, P. E. J., Brüggén, M., Forman, W. R., Böhringer, H., Werner, N., & Finoguenov, A. 2009, A&A, 495, 721
- Simionescu, A., et al. 2011, Science, 331, 1576
- Smith, R. K., Brickhouse, N. S., Liedahl, D. A., & Raymond, J. C. 2001, ApJL, 556, L91
- Sun, M., Voit, G. M., Donahue, M., Jones, C., Forman, W., & Vikhlinin, A. 2009, ApJ, 693, 1142
- Takizawa, M., & Mineshige, S. 1998, ApJ, 499, 82
- Takizawa, M. 1998, ApJ, 509, 579
- Takizawa, M. 1999, ApJ, 520, 514
- Tamura, T., et al. 2008, PASJ, 60, 317
- Tawa, N. 2008, PhD Thesis, University of Osaka
- Tawa, N., et al. 2008, PASJ, 60, S11
- Taylor, G. B., Perley, R. A., Inoue, M., Kato, T., Tabara, H., & Aizu, K. 1990, ApJ, 360, 41
- Tozzi, P., & Norman, C. 2001, ApJ, 546, 63
- Trentham, N., & Mobasher, B. 1998, MNRAS, 299, 488
- Urban, O., Werner, N., Simionescu, A., Allen, S. W., & Böhringer, H. 2011, MNRAS, 414, 2101
- Vazza, F., Brunetti, G., Kritsuk, A., Wagner, R., Gheller, C., & Norman, M. 2009, A&A, 504, 33
- Vikhlinin, A., Markevitch, M., Murray, S. S., Jones, C., Forman, W. & Van Speybroeck, L. 2005, ApJ, 628, 655
- Vikhlinin, A., Kravtsov, A., Forman, W., Jones, C., Markevitch, M., Murray, S. S., & Van Speybroeck, L. 2006, ApJ, 640, 691
- Voit, G. M., Kay, S. T., & Bryan, G. L. 2005, MNRAS, 364, 909
- Wise, M. W., McNamara, B. R., Nulsen, P. E. J., Houck, J. C., & David, L. P. 2007, ApJ, 659, 1153
- Yoshino, T., et al. 2009, PASJ, 61, 805
- Zhang, Y.-Y., Okabe, N., Finoguenov, A., et al. 2010, ApJ, 711, 1033